Scientific
Research
Publishing

A Comparative Study of Williamson Hybrid Nanofluid Flow Consisting of Cu, GaN, and Al₂O₃ Nanoparticles in Ethylene Glycol over a Stretching Sheet with Suction/Injection and Heat Source/Sink

Mamidala Jyotshna[1]* ⓘ, Vadlakonda Dhanalaxmi[2]

[1]Department of Mathematics, Maturi Venkata Subba Rao Engineering College (Affiliated to Osmania University), Hyderabad, India
[2]Department of Mathematics, University College of Technology, Osmania University, Hyderabad, India
Email: *mamidala.jyotsna@gmail.com

Abstract

Several new techniques in the field of heat transfer in fluids have opened new avenues for studying the heat transfer effects in nanofluids and thermodynamic flow parameters, leading to novel applications. There have been studies on nanofluids, including metal, ceramic and magnetic nanoparticles mixed with base fluids such as Water, Kerosene, and Ethylene glycol. However, research on fluids employing semiconductor nanoparticles as supplements to base fluids to generate nanofluids and hybrid nanofluids is limited. For the investigation, Gallium nitrite, a binary semiconductor with excellent heat convection, is together with Cu metal nanoparticles and Al₂O₃ ceramic nanoparticles separately in the base fluid Ethylene glycol (EG) to form hybrid nanofluids. The effects of convective boundary conditions, thermal radiation, heat source/sink, suction/injection, and activation energy on three-dimensional Williamson MHD hybrid nanofluid flow of Cu + GaN + EG, Al₂O₃ + GaN + EG, and Cu + Al₂O₃ + EG are investigated on a stretched sheet with porosity. A similarity transformation is performed on the governing equations to transform them into dimensionless ordinary differential equations ODEs. Numerical analysis is carried out in MATLAB utilizing bvp5c and the shooting technique. The variations of velocity, temperature, and concentration profiles as a function of different physical effects are presented graphically with dimensionless parameters and explained the variations scientifically. As varied with different parameters, the values of the Skin-friction coefficient, Nusselt number, and Sherwood number are mentioned in the table.

1. Introduction

For the last two decades, scientists have investigated fluid flow and heat transfer
processes aiming at higher heat transfer efficiency. Therefore, the focus has been
on improving the heat exchange process by adopting new heat transfer methods
and fluids with different additives. In the process, the attention shifted toward
Power law, Casson, Williamson, and Maxwell types of fluids. Subsequently, the
fluids prepared by dispersing nanoparticles of size less than 100 nm, known as
nanofluids, are recognized as better fluids than base fluids like Water, Kerosene,
Ethylene glycol, etc. In modern technology, the performance of nanofluids paved
the way for many applications, such as cooling processes, lubrication in automo-
biles, food processing, micro-electronic cooling refrigeration, and power genera-
tion. Sakiadis [1] and Crane [2] were the first to introduce the fluid flow past a
stretching surface. Masuda *et al.* [3], for the first time, studied on change in ther-
mal conductivity and viscosity of liquid by dispersing ultrafine particles. Choi
[4] created the term "nanofluids", used to improve the heat transfer mechanism.
Williamson fluid is the only one of these nanofluids to have a reduced viscosity
at high shear stress rates, demonstrating that its effective density should decrease
independently as the shear rate rises. These fluids have several industrial uses,
including lubrication, spinning machinery, and viscometry. Because of these unique
features, nanofluids are used in multiple industrial areas, such as coolants in
nuclear reactors, heat transfer agents, thermal detectors, solar thermal collectors,
radiators, and microelectronic devices. Hayat [5] discussed different physical pa-
rameters (profiles) variations through graphical representation. Malik *et al.* [6]
used the Williamson fluid model to calculate the numerical solution for the flow
of a fluid with variable thermal conductivity in variable mode and heat transfer
effect along a stretched cylinder. Kebede [7] described the heat and mass trans-
port properties of Williamson nanofluid flow. Later, several researchers and scien-
tists built on this concept to produce astounding achievements in flow and heat
transfer. [8] [9] [10] [11]. Kuttan *et al.* [12] investigated the influence of four
nanoparticles on the flow of a boundary layer via a stretched surface. Vinita and
Poply [13] and Mondal *et al.* [14] have studied the effect of heat production on
nanofluid flow via a stretched cylinder.

All the investigations on nanofluids failed in identifying suitable nanofluid(s)
with an elevated heat transfer rate necessary for bulk production companies. To
address this deficiency, hybrid nanofluids are developed by combining more
than one variety of nanoparticles in a base fluid [15]. The thermal performance
of hybrid nanofluids is characterized by various factors like thermal conduction,

thickness and size of nanomaterials, heat and concentration of the molecules, and many more. It was also experimentally verified that hybrid nanofluids give better thermal flow in base fluids. These hybrid nanofluids have better thermal properties compared to base fluids and nanofluids. Recently, Khan *et al.* [16] considered a fluid flow consisting of silicon dioxide and molybdenum disulfide to know the effect of heat source or sink on thermal properties. Hossiany and Eid [17] investigated propylene glycol-water-based fluid's heat transfer mechanism and fluid flow with hybrid nanoparticle suspension [15]. Muhammad Ramzan *et al.* [18] examined the flow of nanofluids, including EG and $NiZnFe_2O_4$ nanoparticles, across a curved surface and found that the Schmidt and Prandtl numbers decreased the fluid concentration.

Aluminum oxide (Al_2O_3) nanoparticles have received much interest due to their considerable increase in burning rate, coolant, ignition time, and temperature. In addition, Al_2O_3 has a unique far-infrared emission, and its nanoparticles have remarkable uses in aerospace due to high energy release during the oxidation process and heat shielding coatings in aircraft, among other things. Furthermore, Al_2O_3 nanoparticles are used in liquid form to increase ceramic density, fracture toughness, creep resistance, wear resistance, smoothness, and other properties in polymers, ceramics, rubber, and refractory goods. Sriharan *et al.* [19] investigated the heat transfer performance of metal oxide base nanofluids experimentally and discovered that Al_2O_3-deionized water nanofluids had a higher heat transfer coefficient. Umair Rashid and Adnan Ibrahim [20] have studied the impacts of nanoparticle shape on Al_2O_3-water nanofluid flows and report that the heat transfer augmentation in laminar shapes nanoparticles is more than in other shapes of nanoparticles.

Copper, in its nanomaterial form, has many uses in mechanical and thermal aspects. The exceptional physical properties of copper are due to its excellent heat and electrical conductivities, good machinability, non-magnetic, practically insoluble in water, and retention of mechanical and electrical properties at cryogenic temperatures. Among the other metals, copper has almost the second highest value of specific heat capacity. Gupta *et al.* [21] have enumerated magnetohydrodynamic three-dimensional boundary layer flow and heat transfer of water-driven copper and alumina nanoparticles induced by convective conditions. Later, Eastman *et al.* [22] showed that copper nanoparticles are more efficient than their oxide nanoparticles immersed with base fluids to enhance heat transfer. Elcio Nogueira [23] has sought an analytical solution for obtaining the outlet temperature of the hot and cold fluids in shell and tube heat exchangers consisting of Ethylene glycol and water as base fluids and CuO nanoparticles. He has observed the flow laminarization effect.

GaN, a III - V compound, is a very hard, mechanically stable wide band gap semiconductor material with high heat capacity and thermal conductivity. GaN semiconductor is recognized as one of the most promising materials for fabricating optical devices in the visible short wavelength and UV region. It has a

high melting temperature of >1600°C and a density as high as 6100 kg/m³. The very high breakdown voltages, electron mobility, and saturation velocity of GaN have also made it an ideal candidate for high-power and high-temperature microwave applications. They are also utilized in military electronic radars [24]. Due to their exceptional chemical, physical, and mechanical capabilities arising from size impact, GaN semiconductor nanoparticles are widely employed in the fabrication of solar cells, photo sensors, and significant electronic industries [25] [26] [27] of its suitable electronic applications, good thermal conductivity, and high heat capacity, one can predict its good prominence and participation in studying heat flow transfer in fluids.

Researchers have examined the flow of nanofluids containing magnetic (Fe_2O_3, $ZnFe_2O_3$, $CoFe_2O_3$), nonmetallic (MgO, TiO_2, Al_2O_3), and metallic (Cu, Ag, Au) nanoparticles under a variety of conditions, including stretching sheets, inclined magnetic fields, nonlinearly stretched porous sheets, thermal flux, etc. [28]-[33]. Likewise, very few papers have been published on ZnO [34] [35] and CdTe [36] semiconductor nanofluids, but the studies on hybrid nanofluids consisting of semiconductor compound nanoparticles (SCNPs) as one of the constituents in nanofluids are not found in the literature. Therefore, it is perceived that the results of heat transfer of hybrid nanofluids consisting of SCNPs under different external forces and boundary conditions are exciting and may acquire industrial applications. The envisaged industries are those producing hydraulic brake fluids and pharmaceutical vehicles. Hence, in the present analysis, attempts at the study of Williamson hybrid nanofluid, consisting of Cu + GaN, Al_2O_3 + GaN nanoparticles in the base fluid Ethylene glycol, running over a linearly stretched porous sheet under the influence of the magnetic field, heat source/sink, suction/injection, radiation, and Arrhenius activation energy. The results are compared with those of hybrid nanofluids consisting of Cu + Al_2O_3 nanoparticles in order to understand the changes in temperature, velocity, and concentration profiles caused with the inclusion of GaN semiconductor nanoparticles as a part of hybrid nanofluids.

2. Geometrical Model of the Problem

A steady, incompressible three-dimensional boundary layer Williamson hybrid nanofluid with convective boundary condition is assumed to run over a stretched porous sheet in the *xy*-plane with the velocity components *u, v,* and *w* along the *x, y,* and *z* directions, respectively. The surface is assumed to be stretching at a rate proportionate to its distance from the origin along the *x* and *y* directions, as shown in Figure 1. A uniform magnetic field of strength B_o is applied along the positive *z*-direction.

3. Mathematical Model

1) The governing equations:
To construct a mathematical model for the flow of a viscous nanofluid across
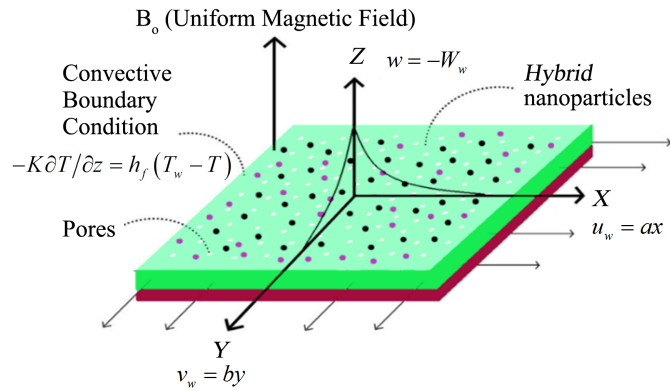
Figure 1. Geometrical diagram representing the problem.

a stretched sheet in three-dimension, with an incompressible steady-state laminar boundary layer flow, the conditions assumed are.

- The sheet is linearly stretched along the x- and y-axes with the velocities $u_w(x) = ax$ and $v_w(y) = by$, where a and b are stretching constants which are displayed in **Figure 1**, representing the problem.
- The ambient fluid's temperature and concentration were indicated, respectively, by the letters T_∞ and C_∞ (at its free surface).
- Similarly, the uniform surface temperature (T_w) and concentration (C_w) of the sheet corresponding to the plane $z = 0$ are represented by T_w and C_w respectively. Here, the z-axis is normal to the flow which is constrained to $z > 0$.
- Cu, Al$_2$O$_3$, and GaN nanoparticles of a homogeneous size and shape are combined with ethylene glycol (EG) as the base fluid to create the Williamson nanofluid flow.
- The stretched surface is subjected transversely, or along the z-direction, to the magnetic field of uniform field strength B_o. Since the fluid's Reynolds number is regarded as low, the generated magnetic field in the liquid is insignificant.
- The linear stretched sheet has a small pressure gradient which can be neglected ($\partial p/\partial x = 0$).

When suction/injection, heat source or sink, thermal radiation, and activation energy are present, the Williamson hybrid nanofluid's heat transport mechanism is examined using convection boundary conditions on a linearly stretched permeable sheet applied with a uniform magnetic field. The thermophysical characteristics of the nanoparticles and base fluids employed in the current problem are displayed in **Table 1**. **Table 2** provides the mathematical equations for several nanofluid physical parameters.

The model of Williamson fluid is taken [40] [41] [42] as

$$\dot{S} = -\dot{p}I + \tau, \tag{1}$$

$$\tau = \left[\mu_\infty + \frac{\mu_0 - \mu_\infty}{1 - \Gamma\dot{\gamma}} \right] A_1, \tag{2}$$

Table 1. Thermo-physical properties of the fluid and nanoparticles.

Physical parameters	Ethylene glycol $(C_2H_6O_2)$ [38]	Copper (Cu) [19]	Alumina (Al_2O_3) [19]	Gallium nitride (GaN) [39]
ρ (kg/m³)	1115	8933	3970	6150
C_p (J/kgK)	2430	385	375	431
k (W/mK)	0.253	400	40	230

Table 2. Mathematical equations of thermophysical properties of nanofluids and hybrid nanofluids [28] [37].

Properties	Equation(s) for nanofluids	Equation(s) for hybrid nanofluids
Thermal Diffusivity	$\alpha_{nf} = \dfrac{k_{nf}}{(\rho c_p)_{nf}}$	$\alpha_{hnf} = \dfrac{k_{hnf}}{(\rho c_p)_{hnf}}$
Dynamic Viscosity	$\mu_{nf} = \dfrac{\mu_f}{(1-\Phi)^{2.5}}$	$\mu_{hnf} = \dfrac{\mu_f}{(1-\Phi_1)^{2.5}(1-\Phi_2)^{2.5}}$
Thermal conductivity	$K_{nf} = K_f \left(\dfrac{K_s + 2K_f - 2\Phi(K_f - K_s)}{K_s + 2K_f + \Phi(K_f - K_s)} \right)$	$K_{hnf} = K_{bf}\left(\dfrac{K_2 + 2K_{bf} - 2\Phi(K_{bf} - K_2)}{K_2 + 2K_{bf} + \Phi(K_{bf} - K_2)} \right)$ *Where* $K_{bf} = K_f\left(\dfrac{K_1 + 2K_f - 2\Phi(K_f - K_1)}{K_1 + 2K_f + \Phi(K_f - K_1)} \right)$
Density	$\rho_{nf} = (1-\Phi)\rho_f + \Phi\rho_s$	$\rho_{hnf} = \left[(1-\Phi_2)\left(1-\Phi_1 + \Phi_1\dfrac{\rho_1}{\rho_f}\right) + \Phi_2\dfrac{\rho_2}{\rho_f} \right]\rho_f$
Heat capacity	$(\rho C_p)_{nf} = (1-\Phi)(\rho C_p)_f + \Phi(\rho C_p)_s$	$(\rho C_p)_{hnf} = \left[(1-\Phi_2)\left(1-\Phi_1 + \Phi_1\dfrac{(\rho C_p)_1}{(\rho C_p)_f}\right) + \Phi_2\dfrac{(\rho C_p)_2}{(\rho C_p)_f} \right](\rho C_p)_f$
Kinematic viscosity *Mass diffusivity*	$v_f = \dfrac{\mu_f}{\rho_f}$	$D_{hnf} = (1-\Phi_1)^{2.5}(1-\Phi_2)^{2.5}D_f$

where τ —extra stress tensor; $\dot{S}$ —Cauchy stress tensor; I—identity vector; $\dot{p}$ —Pressure; μ_0 —limiting viscosity at zero shear rate; A_1 —first Rivlin-Erickson tensor; μ_∞ —limiting viscosity at infinity shear rate; $\Gamma > 0$ —time constant;

$$\dot{\gamma} = \sqrt{\frac{1}{2}trace\left(A_1^2\right)}, \tag{3}$$

Here in this case, they are all restrained by $\mu_\infty = 0$ and $\Gamma\dot{\gamma} < 1$.
Thus, τ equal to

$$\tau = \left[\frac{\mu_0}{1-\Gamma\dot{\gamma}}\right]A_1, \tag{4}$$

Using binomial expansion to Equation (4), given as

$$\tau = \mu_0\left[1+\Gamma\dot{\gamma}\right]A_1. \tag{5}$$

The governing equations [42] [43] [44] [45] are as follows

$$\frac{\partial u}{\partial x}+\frac{\partial v}{\partial y}+\frac{\partial w}{\partial z}=0 \tag{6}$$

$$u\frac{\partial u}{\partial x}+v\frac{\partial u}{\partial y}+w\frac{\partial u}{\partial z}=\frac{\mu_{hnf}}{\rho_{hnf}}\frac{\partial^2 u}{\partial z^2}+\sqrt{2}\frac{\mu_{hnf}}{\rho_{hnf}}\Gamma\frac{\partial u}{\partial z}\frac{\partial^2 u}{\partial z^2}-\frac{\sigma B_o^2}{\rho_{hnf}}u-\frac{\mu_{hnf}}{\rho_{hnf}K_p}u \tag{7}$$

$$u\frac{\partial v}{\partial x}+v\frac{\partial v}{\partial y}+w\frac{\partial v}{\partial z}=\frac{\mu_{hnf}}{\rho_{hnf}}\frac{\partial^2 v}{\partial z^2}+\sqrt{2}\frac{\mu_{hnf}}{\rho_{hnf}}\Gamma\frac{\partial v}{\partial z}\frac{\partial^2 v}{\partial z^2}-\frac{\sigma B_o^2}{\rho_{hnf}}v-\frac{\mu_{hnf}}{\rho_{hnf}K_p}v \tag{8}$$

$$u\frac{\partial T}{\partial x}+v\frac{\partial T}{\partial y}+w\frac{\partial T}{\partial z}=\alpha_{hnf}\frac{\partial^2 T}{\partial z^2}-\frac{1}{\left(\rho c_p\right)_{hnf}}\frac{\partial q_r}{\partial z}+\frac{Q_o\left(T-T_\infty\right)}{\left(\rho c_p\right)_{hnf}} \tag{9}$$

$$u\frac{\partial C}{\partial x}+v\frac{\partial C}{\partial y}+w\frac{\partial C}{\partial z}=D_B\frac{\partial^2 C}{\partial z^2}-K_o^2\left(c-c_\infty\right)\left(\frac{T}{T_\infty}\right)^m\exp\left(\frac{-E_a}{kT}\right) \tag{10}$$

By Rosseland approximation, the radiative heat flux $\dfrac{\partial q_r}{\partial z}$ [46] is given by

$$\frac{\partial q_r}{\partial z}=\frac{16\sigma^* T_\infty^3}{3k^*}\frac{\partial^2 T}{\partial z^2}.$$

2) Boundary conditions

According to Geethan Kumar [42], the boundary conditions for the velocity, temperature, and concentration fields are:

$$z=0:u=u_w=ax, v=v_w=by, w=-W_w, -K\frac{\partial T}{\partial z}=h_f\left(T_w-T\right), C\to C_w$$
$$z\to\infty:u\to 0, v\to 0, T\to T_\infty, C\to C_\infty \tag{11}$$

where K—the thermal conductivity and h_f—the heat transfer coefficient.

3) Similarity equations

The similarity transformation equations are

$$u=axf'(\eta), v=ayg'(\eta), w=-\sqrt{av_f}\left(f(\eta)+g(\eta)\right)$$
$$\theta(\eta)=\frac{T-T_\infty}{T_w-T_\infty}, \eta=z\sqrt{\frac{a}{v_f}}, \phi(\eta)=\frac{C-C_\infty}{C_w-C_\infty} \tag{12}$$

After using the above transformations, the continuity Equation (6) is identically satisfied, whereas the Equations (7)-(10) are transformed into 2nd and 3rd-order ODE's given below.

$$\left(1+L_1L_2\lambda_1 f''\right)f'''=L_1L_2\left(f'^2-\left(f+g\right)f''\right)+MfL_2+Kf' \tag{13}$$

$$\left(1+L_1L_2\lambda_2 g''\right)g'''=L_1L_2\left(g'^2-\left(f+g\right)g''\right)+Mg'L_2+Kg' \tag{14}$$

$$\left(\frac{k_{hnf}}{k_f}+\frac{4}{3R}\right)\theta''=-Pr\left(\left(f+g\right)\theta'L_3+Q\theta\right) \tag{15}$$

$$L_2\phi'' = -(Sc)\left(\sigma\phi(\theta\delta+1)^m \exp\left(\frac{-E}{1+\delta\theta}\right) - \phi'(f+g)\right) \tag{16}$$

Here, f, g, ϕ, θ are the functions of η,

$$L_1 = \left((1-\Phi_2)\left(1-\Phi_1+\Phi_1\frac{\rho_1}{\rho_f}\right)+\Phi_2\frac{\rho_2}{\rho_f}\right),$$

$$L_2 = (1-\Phi_1)^{2.5}(1-\Phi_2)^{2.5},$$

$$L_3 = \left((1-\Phi\phi_2)\left(1-\Phi_1+\Phi_1\frac{(\rho C_p)_1}{(\rho C_p)_f}\right)+\Phi_2\frac{(\rho C_p)_2}{(\rho C_p)_f}\right).$$

The transformed boundary conditions given as

$$\text{at } \eta = 0: f'(\eta) = 1, f(\eta) = S - g(\eta), g(\eta) = 0, g'(\eta) = \alpha,$$
$$\theta'(\eta) = -Bi(1-\theta(\eta)), \phi(\eta) = 1 \tag{17}$$
$$\text{at } \eta \to \infty: f'(\eta) \to 0, g'(\eta) \to 0, \theta(\eta) \to 0, \phi(\eta) \to 0$$

Here "prime" stands for the coefficient of differentiation w.r.t η.

The dimensionless parameters are listed as

$$\lambda_1 = \Gamma x\sqrt{\frac{a^3}{2\nu}}, \lambda_2 = \Gamma y\sqrt{\frac{a^3}{2\nu}}, M = \frac{\sigma B_o^2}{\rho_f a}, P_r = \frac{(\rho c_p)_f \nu_f}{K_f},$$

$$S_c = \frac{\nu_f}{D_B}, R = \frac{4\sigma^* T_\infty^3}{k^* K_f}, \alpha = \frac{b}{a}, \delta = \frac{T_w - T_\infty}{T_\infty}, \sigma = \frac{K_o^2}{a}, \tag{18}$$

$$E = \frac{E_a}{kT_\infty}, Q = \frac{Q_o}{a(\rho c_p)_f}, S = \frac{W_w}{\sqrt{a\nu_f}}$$

The heat transfer rates in this study, which are represented by the Skin-friction coefficient C_f, Nusselt number Nu, and Sherwood's number S_h, are defined as (see, for example, [18] [44]) are defined as

$$C_{fx} = \frac{\tau_{xz}}{\rho_f \nu_w^2}, C_{fy} = \frac{\tau_{yz}}{\rho_f \nu_w^2}, Nu = \frac{-xq_w}{T_w - T_\infty} \text{ and } S_h = \frac{-xJ_w}{C_w - C_\infty} \tag{19}$$

Here, shear stress at the surfaces is given as $\tau_{xz} = \mu_{hnf}\left[\frac{\partial u}{\partial z} + \frac{\Gamma}{\sqrt{2}}\left(\frac{\partial u}{\partial z}\right)^2\right]_{z=0}$,

$\tau_{yz} = \mu_{hnf}\left[\frac{\partial v}{\partial z} + \frac{\Gamma}{\sqrt{2}}\left(\frac{\partial v}{\partial z}\right)^2\right]_{z=0}$, $q_w = -\left[k_{hnf} + \frac{16\sigma^* T_\infty^3}{3k^*}\right]\left(\frac{\partial T}{\partial z}\right)_{z=0}$ the wall heat,

and

$$J_w = -D_{hnf}\left(\frac{\partial C}{\partial z}\right)_{z=0} \tag{20}$$

the mass transfers.

By using Equations (19) and (20), the dimensionless "Skin-friction coefficient, Nusselt number, and Sherwood number" [47] [48] [49] [50] are simplified as

$$2(Re_x)^{1/2} C_{fx} = \frac{1}{L_2}\left[f''(0)+\frac{\lambda}{2}\left(f''(0)\right)^2\right]$$

$$\alpha^{3/2} 2(Re_x)^{1/2} C_{fy} = \frac{1}{L_2}\left[g''(0)+\frac{\lambda}{2}\left(g''(0)\right)^2\right]$$

$$(Re_x)^{-1/2} Nu_x = -\left[\frac{k_{hnf}}{k_f}+\frac{4}{3}R\right]\theta'(0)$$

$$(Re_x)^{-1/2} Sh = -\frac{D_{hnf}}{D_f}\phi'(0)$$

(21)

$Re_x = \dfrac{u_w x}{v_f}, Re_y = \dfrac{v_w y}{v_f}$ are Reynold's numbers.

4. Numerical Method and Validation

To validate the obtained results, the MATLAB built-in bvp5c program is employed. The RK-45 order approach is used to direct the shooting technique toward the boundary conditions while accounting for the lacking initial conditions. The numerical bvp5c was generated using the concept of a finite-difference method, and the results were compared in Table 3.

$$f_1' = f_2, f_2' = f_3 \text{ and } f_3' = \frac{L_1 L_2\left(f_2^2 -\left(f_1+f_4\right)f_3\right)+Mf_2 L_2 + Kf_2}{1+L_1 L_2 \lambda_1 f_3}$$

(22)

$$f_4' = f_5, f_5' = f_6 \text{ and } f_6' = \frac{L_1 L_2\left(f_5^2 -\left(f_1+f_4\right)f_6\right)+Mf_5 L_2 + Kf_5}{1+L_1 L_2 \lambda_2 f_6}$$

(23)

$$f_7' = f_8, f_8' = -\frac{Pr\left(\left(f_1+f_4\right)f_8 L_3 + Qf_7\right)}{\dfrac{k_f}{k_{hnf}}+\dfrac{4}{3R}}$$

(24)

$$f_9' = f_{10}, f_{10}' = -\frac{Sc\left(\sigma f_9\left(f_7\delta+1\right)^m \exp\left(\dfrac{-E}{1+\delta f_7}\right)-\left(f_1+f_4\right)f_{10}\right)}{L_2}$$

(25)

Table 3. Attestation of Skin friction ($C_f Re_x^{1/2}$) results for various values of the magnetic field fixed values $K = \lambda_1 = \lambda_2 = \Phi = Pr = R = Q = Sc = E = \sigma = \delta = \alpha = m = S = 0$.

M	Present result	Amel A. Aladrous et al. [46]	Oyelakin et al. [51]
	$-C_f Re_x^{1/2}$	$-C_f Re_x^{1/2}$	$-C_f Re_x^{1/2}$
0	1.000008	1.00001	1.0000097
1	1.414213	1.41421	1.4142105
5	2.449490	2.44949	2.4494932
50	7.141428	7.14143	7.1414259
100	10.049875	10.0499	10.049894
500	22.383029	22.383	22.383134

The converted initial conditions are

$$f_2(0) = 1, f_1(0) = S - f_4(0), f_4(0) = 0, f_5 = \alpha, f_8 = -Bi(1 - f_7), f_9 = 1$$

$$f_2 \to 0, f_5 \to 0, f_7 \to 0, f_9 \to 0 \tag{26}$$

Analyzing the governing Equations (7)-(10) with boundary conditions (11) is time-consuming. Instead, we used the bvp5c technique to solve the equations numerically in MATLAB. The computations begin with preset values of the physical parameters $\lambda_1 = \lambda_2 = 0.2$, $\sigma = E = \delta = 1.0$, $S = 0.2$, $Sc = 0.6$, $Pr = 6.2$, $R = K = M = Bi = \alpha = 0.5$. Unless otherwise specified, the same base values can be assumed throughout the investigation. Finally, we cross-checked our results with the solutions of [46] [51] (see Table 3) and found extremely strong agreement in the results. Tolerances on the order of 10^{-5} are used in the calculations, and all findings are correct within the stipulated tolerances.

5. Results and Discussion

The flow parameters shown in Figures 2-30 are estimates of species' momentum, energy, and mass [27].

The Numerical results of skin friction drag along x and y directions ($-C_f Re_x^{1/2}$ and $-\alpha^{3/2} C_f Re_y^{1/2}$), Nusselt ($Re_x^{-1/2} Nu$), and Sherwood ($Re_x^{-1/2} Sh$) numbers, the essential emerging parameters, are estimated using different dimensionless parameters for Cu + GaN + EG, Al$_2$O$_3$ + GaN + EG, and Cu + Al$_2$O$_3$ + EG hybrid nanofluids. Their numerical values are shown in Tables 4-6. Skin friction drags in the x and y-direction increase as M, K, α, Φ_2, and S increases but decreases as λ_1 and λ_2 increse for Cu + GaN + EG, Al$_2$O$_3$ + GaN + EG, Cu + Al$_2$O$_3$ + EG. The Nusselt numbers decrease as M, K, λ_1 and λ_2, values increase, whereas they increase with the increase in the values of α, Φ_2, and S for Cu + GaN + EG, Al$_2$O$_3$ + GaN + EG, Cu + Al$_2$O$_3$ + EG. Sherwood numbers rise with the increase in α and S and decrease with the increase in M, K, λ_1 and λ_2.
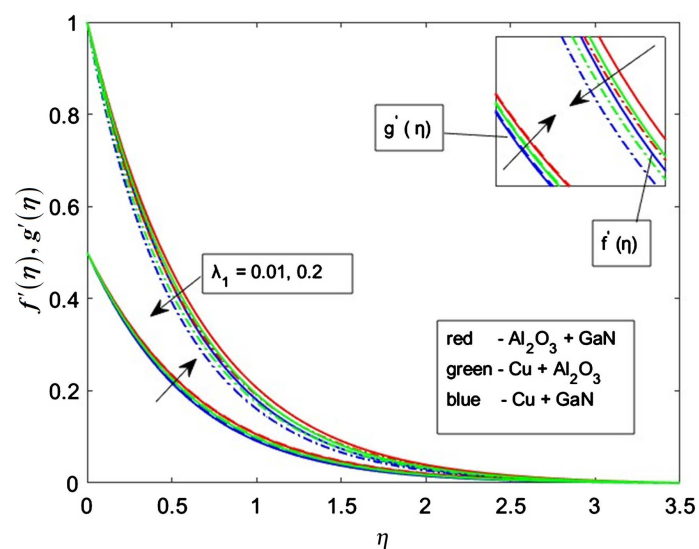

Figure 2. Variation of λ_1 with $f'(\eta)$ and $g'(\eta)$.
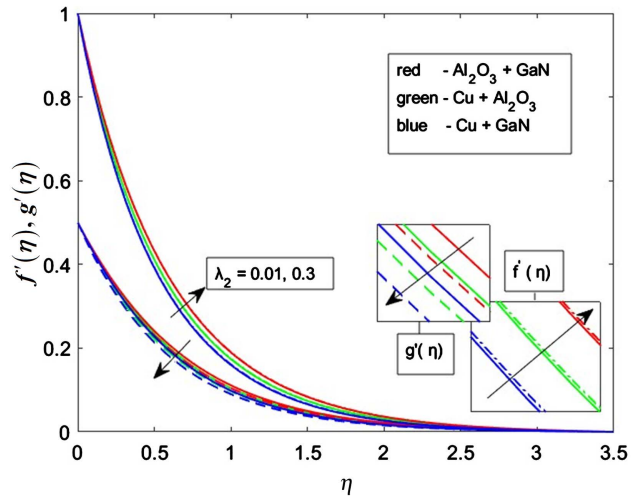
Figure 3. Variation of λ_2 with $f'(\eta)$ and $g'(\eta)$.
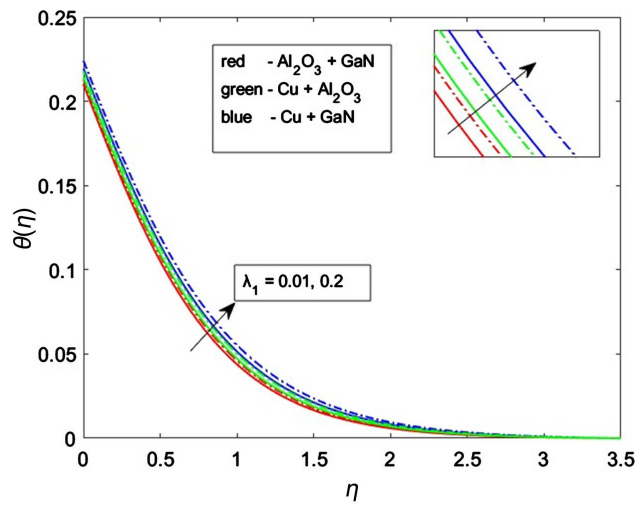
Figure 4. Variation of λ_1 with $\theta(\eta)$.
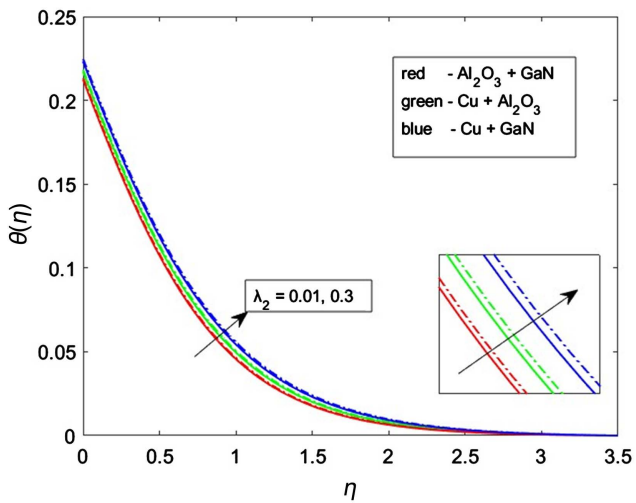
Figure 5. Variation of λ_2 with $\theta(\eta)$.
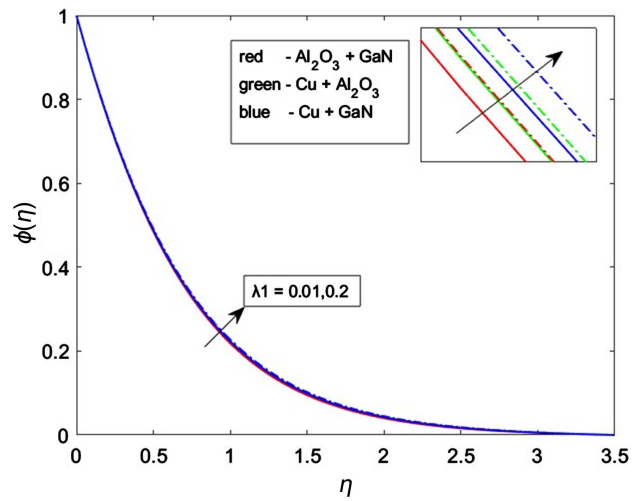
Figure 6. Variation of λ_1 with $\phi(\eta)$.

Figure 7. Variation of λ_2 with $\phi(\eta)$.

Figure 8. Variation of M with $f'(\eta)$ and $g'(\eta)$.
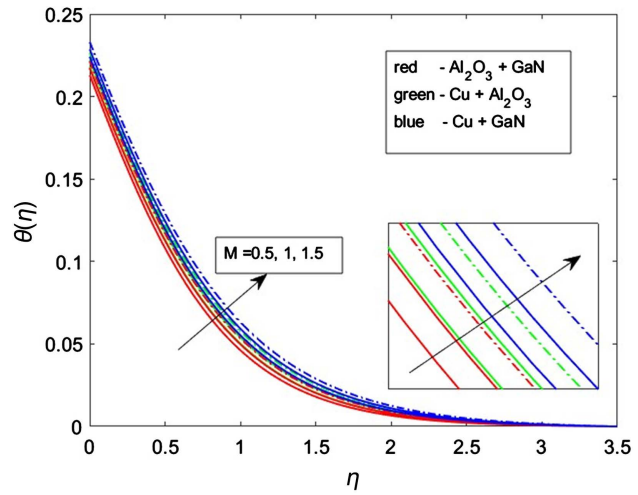
Figure 9. Variation of M with $\theta(\eta)$.
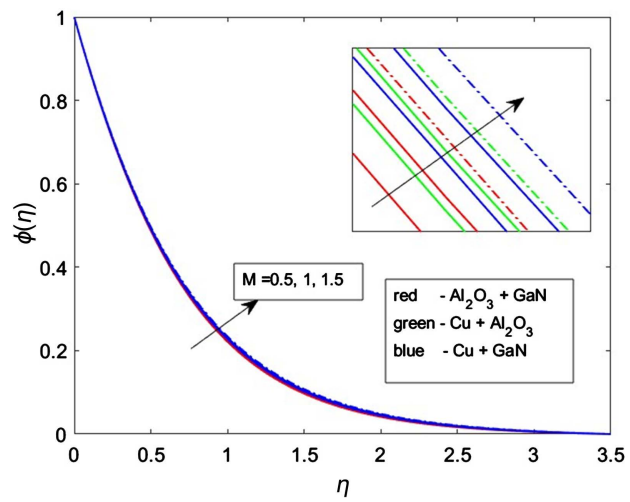
Figure 10. Variation of M on $\phi(\eta)$.
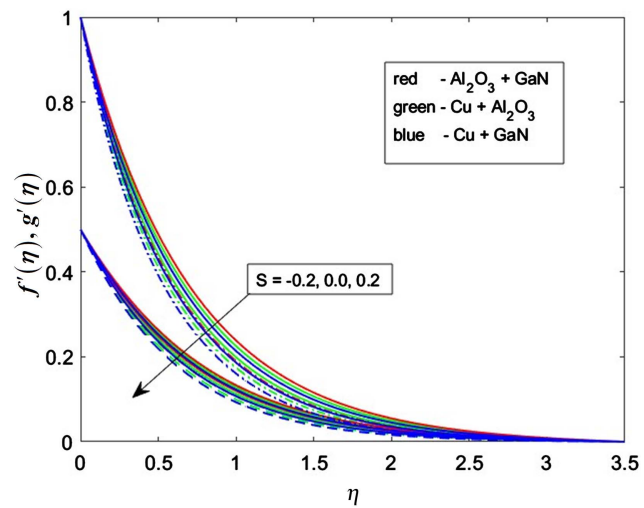
Figure 11. Variation of S on $f'(\eta)$ and $g'(\eta)$.
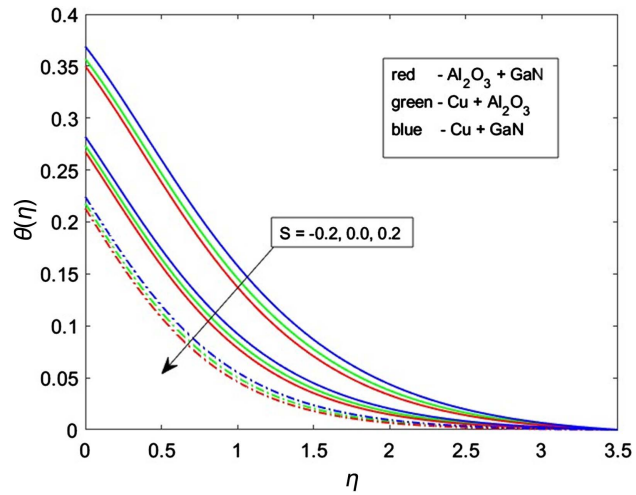
Figure 12. Variation of S on $\theta(\eta)$.
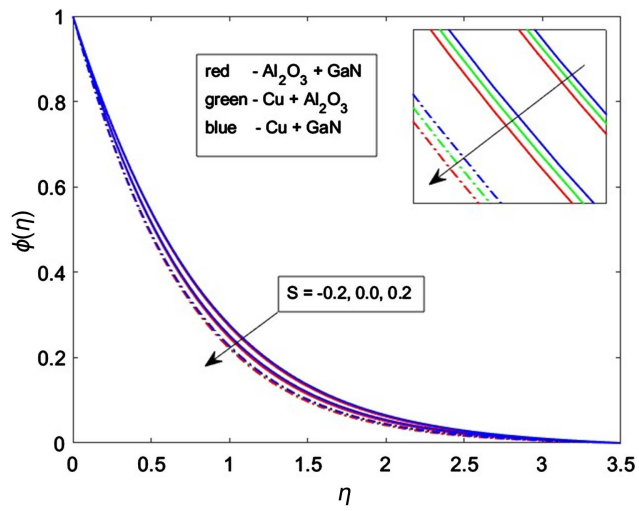
Figure 13. Variation of S on $\phi(\eta)$.
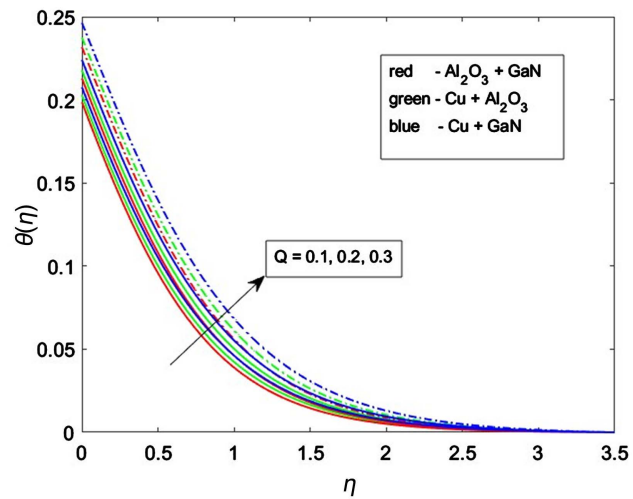
Figure 14. Variation of Q with $\theta(\eta)$.
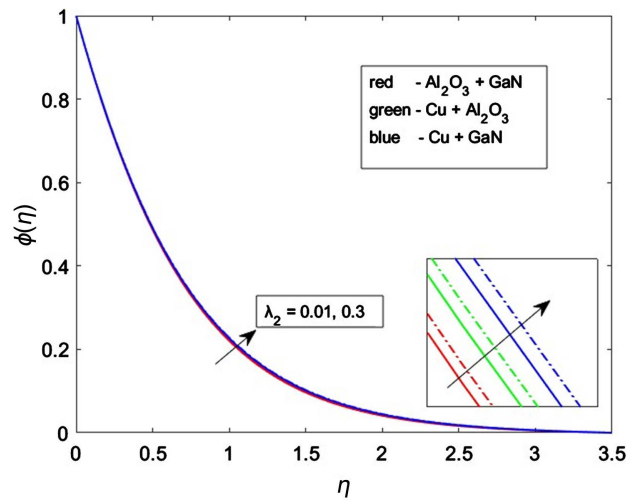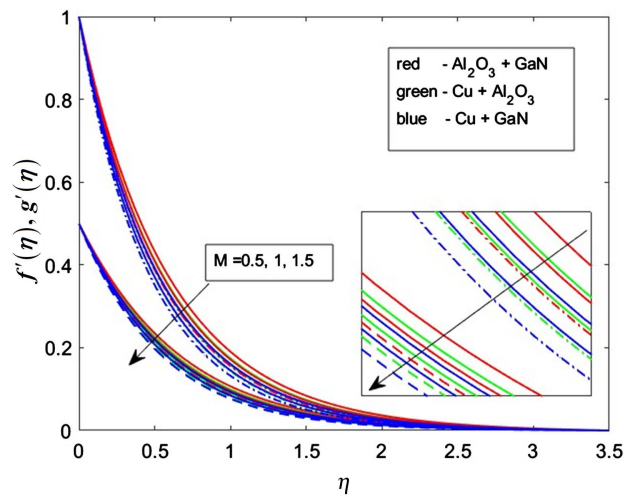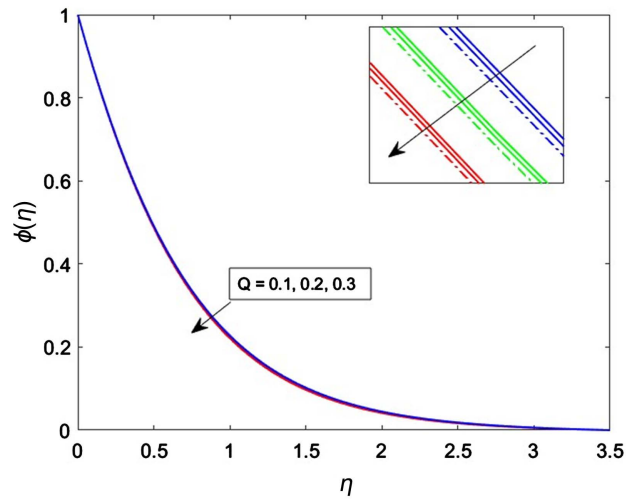
Figure 15. Variation of Q with $\phi(\eta)$.
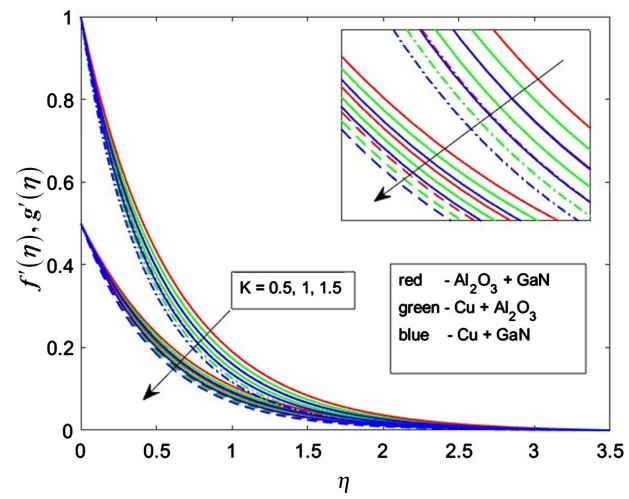
Figure 16. Variation of K with $f'(\eta)$ and $g'(\eta)$.
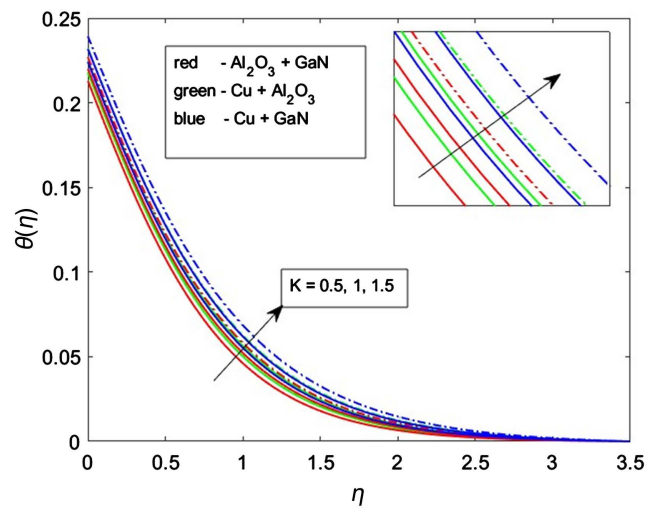
Figure 17. Variation of K with $\theta(\eta)$.
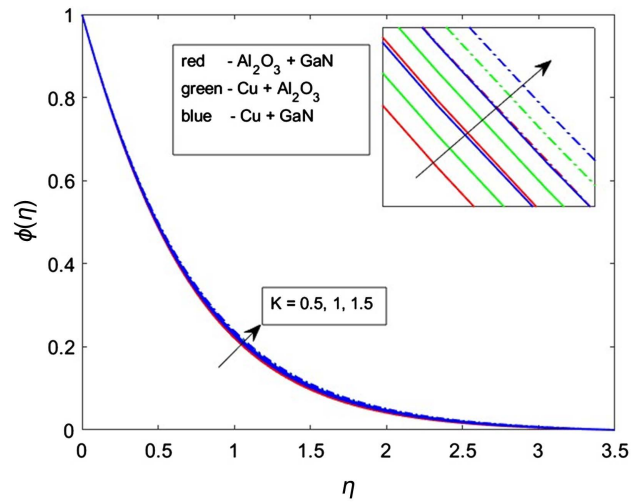
Figure 18. Variation of K with $\phi(\eta)$.
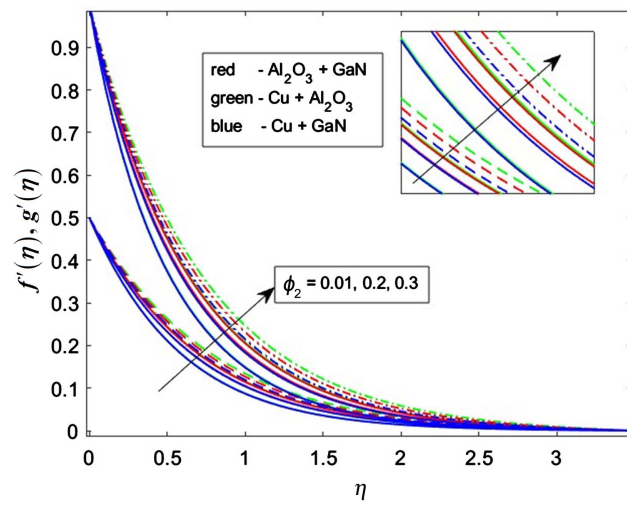
Figure 19. Variation of λ_2 with $f'(\eta)$ and $g'(\eta)$.
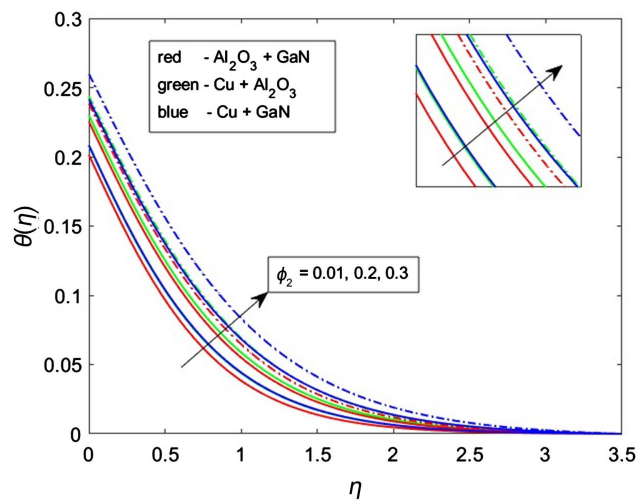
Figure 20. Variation of Φ_2 with $\theta(\eta)$.
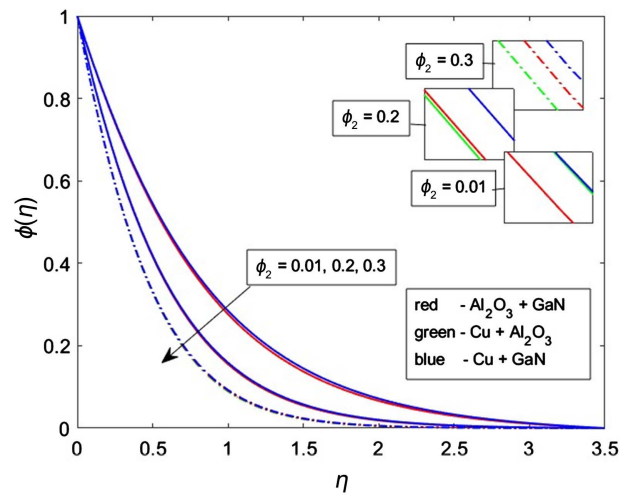
Figure 21. Variation of Φ_2 with $\phi(\eta)$.
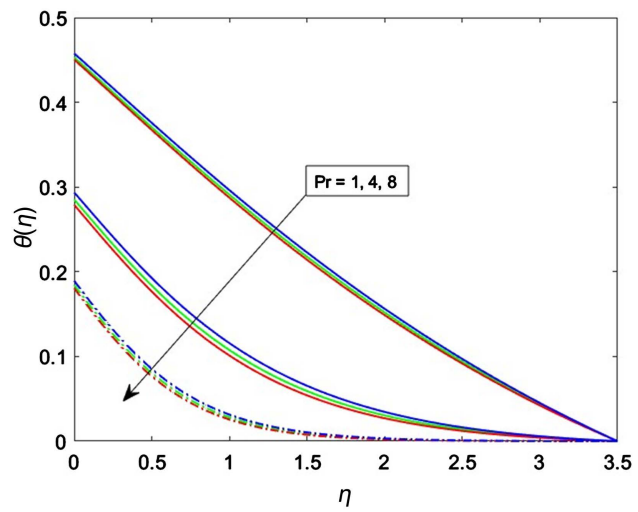
Figure 22. Variation of Pr with $\theta(\eta)$.
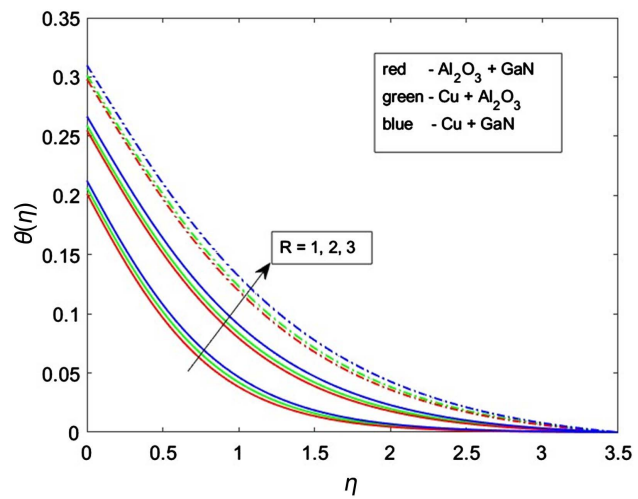
Figure 23. Variation of R with $\theta(\eta)$.
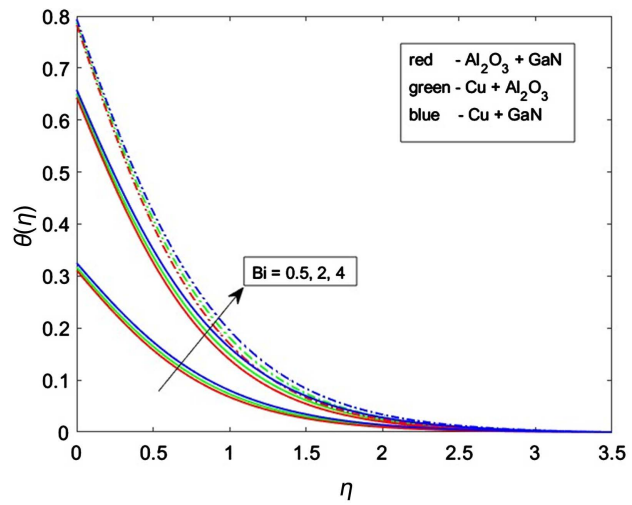
Figure 24. Variation of Bi with $\theta(\eta)$.
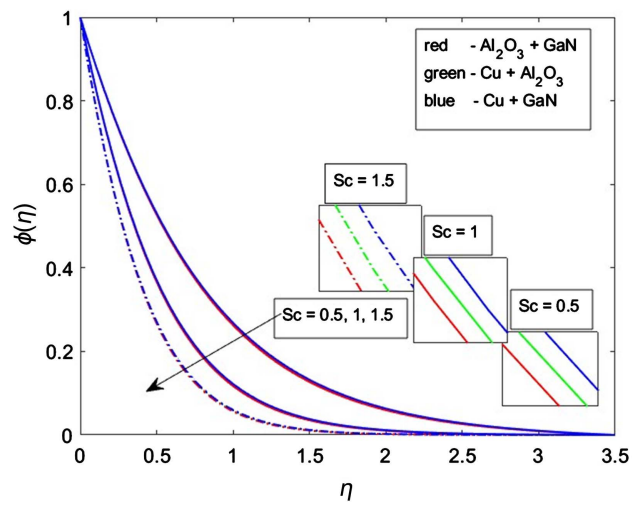
Figure 25. Variation of Sc with $\phi(\eta)$.
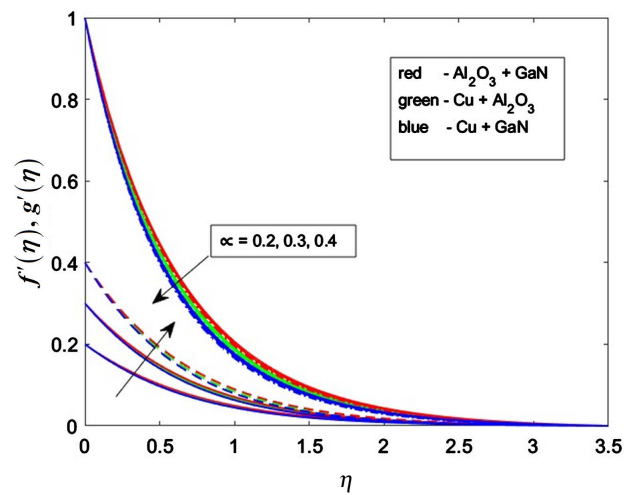
Figure 26. Variation of α with $f'(\eta)$ and $g'(\eta)$.
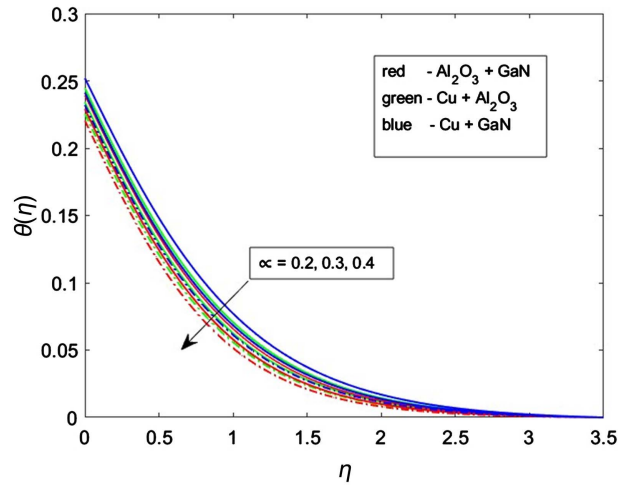
Figure 27. Variation of α with $\theta(\eta)$.
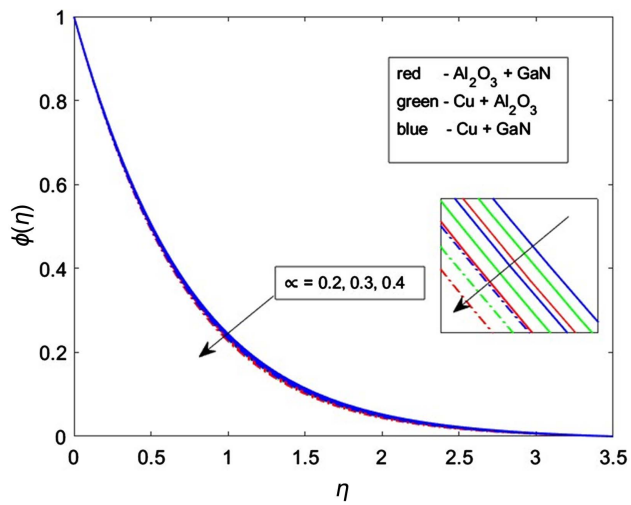
Figure 28. Variation of α with $\phi(\eta)$.
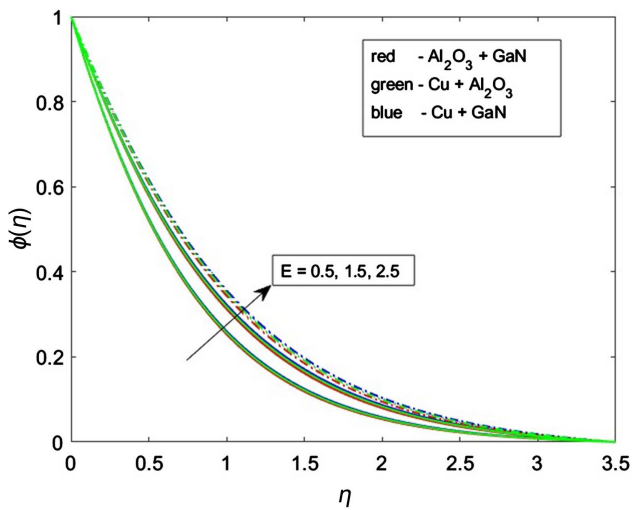
Figure 29. Variation of E with $\phi(\eta)$.
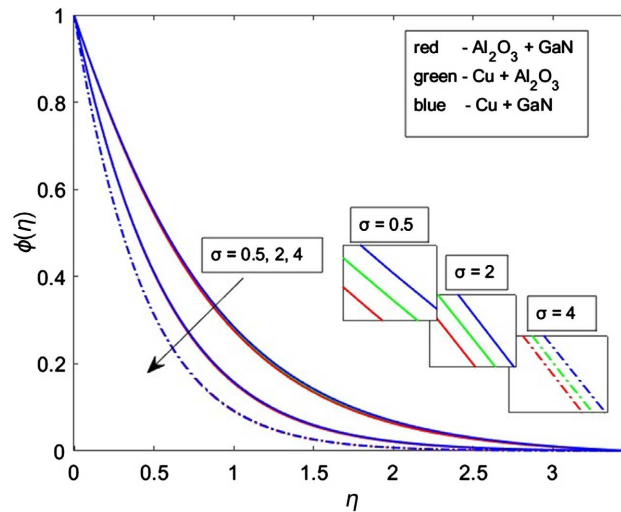
Figure 30. Variation of σ with $\phi(\eta)$.

Table 4. Numerical values of C_f, Nu, and Sh [47] (Cu + GaN + EG).

M	K	λ_1	λ_2	α	Φ_2	S	$-C_f Re_x^{1/2}$	$-\alpha^{3/2} C_f Re_y^{1/2}$	$Re_x^{-1/2} Nu$	$Re_x^{-1/2} Sh$
0.5	0.5	0.2	0.2	0.5	0.1	0.2	2.706523	1.245601	0.660888	0.782796
1							2.862650	1.330278	0.657027	0.779175
1.5							3.011688	1.409604	0.653229	0.775892
	1						2.966669	1.385805	0.654387	0.776866
	1.5						3.209533	1.512307	0.648050	0.771799
	2						3.442693	1.628298	0.641834	0.767386
		0.1					2.727479	1.249840	0.663225	0.785343
		0.3					−4.386579	1.237649	0.656584	0.778115
		0.4					−7.228445	1.234498	0.654630	0.776252
			0.1				2.707869	1.251435	0.661358	0.783279
			0.3				2.704996	1.240697	0.660359	0.782253
			0.4				2.703219	1.237738	0.659750	0.781625
				0.1			2.604230	0.217605	0.626230	0.750588
				0.3			2.656726	0.702639	0.646371	0.766989
				0.7			2.753593	1.839059	0.671914	0.797812
					0.1		2.706523	1.245601	0.660888	0.782796
					0.2		3.327624	1.558642	0.846903	0.699812
					0.3		4.183056	1.990643	1.078223	0.616829
						−0.3	2.155399	0.972829	0.486341	0.640042
						0.0	2.468503	1.129324	0.611575	0.720690
						0.3	2.835500	1.307304	0.679494	0.815986

Table 5. Numerical values of C_f, Nu, and Sh [47] (Al_2O_3 + GaN + EG).

M	K	λ_1	λ_2	α	Φ_2	S	$-C_f Re_x^{1/2}$	$-\alpha^{3/2} C_f Re_y^{1/2}$	$Re_x^{-1/2} Nu$	$Re_x^{-1/2} Sh$
0.5	0.5	0.2	0.2	0.5	0.1	0.2	2.412815	1.146268	0.667269	0.788650
1							2.561286	1.233339	0.663666	0.784657
1.5							2.699239	1.314081	0.660147	0.781081
	1						2.657976	1.289936	0.661217	0.782137
	1.5						2.875979	1.417576	0.655385	0.776685
	2						3.072706	1.533221	0.649733	0.772025
		0.1					2.488416	1.148550	0.668649	0.790374
		0.3					2.320922	1.143336	0.665474	0.786444
		0.4					2.043196	1.138483	0.662508	0.782816
			0.1				2.413560	1.159928	0.667562	0.789003
			0.3				2.412002	1.131719	0.666950	0.788266
			0.4				2.411105	1.116085	0.666599	0.787844
				0.1			2.333368	0.205276	0.634850	0.754277
				0.3			2.374031	0.654366	0.653600	0.771709
				0.7			2.393653	0.895568	0.660919	0.780253
					0.1		2.412815	1.146268	0.667269	0.788650
					0.2		3.086583	1.470141	0.860888	0.702548
					0.3		3.985405	1.912508	1.104231	0.617594
						−0.3	2.011814	0.932691	0.502589	0.641847
						0.0	2.243956	1.056277	0.621017	0.724901
						0.3	2.501433	1.193497	0.684713	0.822655

Table 6. Numerical values of C_f, Nu and Sh [47] (Cu + Al_2O_3 + EG).

M	K	λ_1	λ_2	α	Φ_2	S	$-C_f Re_x^{1/2}$	$-\alpha^{3/2} C_f Re_y^{1/2}$	$Re_x^{-1/2} Nu$	$Re_x^{-1/2} Sh$
0.5	0.5	0.2	0.2	0.5	0.1	0.2	2.555892	1.196879	0.663180	0.785574
1							2.706362	1.282565	0.659517	0.781782
1.5							2.847714	1.362449	0.655930	0.778365
	1						2.805272	1.338520	0.657022	0.779377
	1.5						3.031193	1.465381	0.651066	0.774135
	2						3.239116	1.581031	0.645271	0.769616
		0.1					2.609986	1.200035	0.664969	0.787689
		0.3					2.511849	1.192405	0.660625	0.782601
		0.4					1.287312	1.185303	0.656434	0.777920

Continued

0.1				2.556903	1.207034	0.663551	0.785992
0.3				2.554768	1.186465	0.662770	0.785112
0.4				2.553498	1.175901	0.662310	0.784592
	0.1			2.465822	0.211635	0.630175	0.752275
	0.3			2.512002	0.679143	0.649289	0.769202
	0.7			2.597517	1.755911	0.673822	0.801221
		0.1		2.555892	1.196879	0.663180	0.785574
		0.2		3.063940	1.461475	0.855841	0.703236
		0.3		3.814843	1.843294	1.096296	0.619631
			−0.3	2.084438	0.953546	0.496223	0.640634
			0.0	2.355219	1.093750	0.615971	0.722610
			0.3	2.662517	1.251302	0.681024	0.819185

Table 7 shows the numerical results of Nusselt numbers, which increase with the increase in Pr and Bi but decrease with the increasing values of R and Q. The Sherwood numbers increase with the increased values of R, Bi, Q, Sc, δ, σ, and m, whereas they decrease with the increasing values of Pr and E.

Three different hybrid nanofluids (hnfs) were formed by adding two nanoparticles from Cu, Al_2O_3, and GaN in Ethylene glycol (EG) base fluid, *i.e.*, Al_2O_3 + GaN + EG, Cu + GaN + EG, and Cu + Al_2O_3 + EG abbreviated as AGE, CGE, and CAE respectively are formed. The three hnfs, AGE, CGE, and CAE, are considered in the present study. Figures 2-7 depict the changes in velocity, temperature, and concentration profiles of three nanofluids, AGE, CGE, and CAE nanofluids, for λ_1 = 0.01, 0.2 and λ_2 = 0.01, 0.3 (Williamson parameters) with the boundary layer thickness parameter η. Graphical variations of the results concerning CAE (Cu + Al_2O_3 + EG) hybrid nanofluid (hnf) are included in every figure to compare the results obtained on hnfs consisting of GaN (as one of the nanoparticles) in the nanofluids CGE and AGE. It is noticed from Figure 2 that the axial and transverse velocity profiles $f'(\eta)$ and $g'(\eta)$, decrease and increase respectively with the rise in λ_1. Generally, the williamson parameter λ_1 directly proportional to relaxation time [42]; thus, the fluid velocity increases along the axial direction resulting in a decrease in transverse velocity with a rise in λ_1. Exactly the opposite trend prevails with $f'(\eta)$ and $g'(\eta)$ profiles of AGE, CGE, and CAE hnfs have λ_2 as enhances (Figure 3). As the fluid slows down, the outflow of heat from the fluid reduces, resulting in a rise in the fluid temperature. Figure 4 presents temperature profiles of AGE, CAE, and CGE hnfs for λ_1 = 0.01 and 0.2. Similarly, Figure 5 for λ_2 = 0.01 and 0.3. Both plots indicate that the profiles grow with increasing CGE, CAE, and AGE, demonstrating increased heat energy with increasing Williamson parameters. A rise in λ increases the viscosity of a nanofluid; as a result, the flow of the liquid rises, as

Table 7. Numerical values of *Nu and Sh* number [47] for Cu + GaN + EG, Al$_2$O$_3$ + GaN + EG, and Cu + Al$_2$O$_3$ + EG.

R	Pr	Bi	Q	Sc	E	δ	σ	m	Cu + GaN + EG		Al$_2$O$_3$ + GaN + EG		Cu + Al$_2$O$_3$ + EG	
									$Re_x^{-1/2}Nu$	$Re_x^{-1/2}Sh$	$Re_x^{-1/2}Nu$	$Re_x^{-1/2}Sh$	$Re_x^{-1/2}Nu$	$Re_x^{-1/2}Sh$
1.2	6.2	0.3	0.2	0.6	0.1	1.0	1.0	0.3	0.660888	0.782796	0.667269	0.788650	0.663180	0.785574
0.3									0.177315	0.778416	0.178625	0.784452	0.177398	0.781396
2									0.040950	0.786183	1.052843	0.791933	1.046919	0.788833
	0.7								0.446948	0.802411	0.449236	0.808510	0.401325	0.783309
	4								0.601701	0.788322	0.611328	0.793827	1.880383	0.794801
	8								0.690538	0.780081	0.694760	0.786170	3.338546	0.800587
		1							0.446440	0.795899	1.485796	0.801175	1.465675	0.798368
		1.5							0.742289	0.800406	1.801488	0.805592	1.771990	0.802832
		2							0.940766	0.803317	2.015622	0.808477	1.978766	0.805733
			0.1						0.674924	0.781606	0.679455	0.787638	0.675873	0.784506
			0.3						0.641945	0.784402	0.651358	0.789973	0.646468	0.786981
			0.5						0.567986	0.790576	0.595418	0.794585	0.586182	0.792006
				0.2					0.660888	0.422417	0.667269	0.425378	0.663180	0.423802
				0.4					0.660888	0.618192	0.667269	0.622934	0.663180	0.620429
				0.8					0.660888	0.928119	0.667269	0.934721	0.663180	0.931265
					0.5				0.660888	0.706058	0.667269	0.767997	0.663180	0.709188
					1.5				0.660888	0.579659	0.667269	0.730071	0.663180	0.584072
					2				0.660888	0.542820	0.667269	0.666649	0.663180	0.547842
						0.5			0.660888	0.776686	0.667269	0.779446	0.663180	0.779724
						1.5			0.660888	0.788530	0.667269	0.781837	0.663180	0.791073
						2			0.660888	0.793936	0.667269	0.786436	0.663180	0.796268
							0.5		0.660888	0.647507	0.667269	0.656013	0.663180	0.651590
							1.5		0.660888	0.895916	0.667269	0.900186	0.663180	0.897909
							2		0.660888	0.995027	0.667269	0.998219	0.663180	0.996482
								0.5	0.660888	0.789502	0.667269	0.794812	0.663180	0.791977
								1.5	0.660888	0.825839	0.667269	0.828093	0.663180	0.826608
								2	0.660888	0.845906	0.667269	0.846401	0.663180	0.845689

does particle concentration. **Figure 6** and **Figure 7** show the concentration profiles $\phi(\eta)$ for all the hnfs for various values of λ_1 and λ_2, respectively. Further, the increasing order of concentration profiles of hnfs is CGE, CAE, and AGE.

Figure 8 shows the diminished axial and transverse velocities corresponding to AGE, CAE, and CGE hnfs with the rise in the magnetic parameter (M = 0.5, 1, 1.5). Owing the Lorentz force that emerges due to the application of M, which

opposes the fluid flow, causes a decrease in the axial and transverse velocities. Also, the Lorentz force produces internal friction between fluid particles, causing a rise in the temperature of the fluid and this effect increases with the increase in the magnetic field [42]. The visual evidence is that the velocities of AGE, CAE, and CGE hnfs decrease, and the temperature profiles increase (Figure 9) in the same order. Hence, we understand that CGE hnfs are better cooling agents in cryogenic systems. Further, the increase in the magnetic field causes a temperature rise, implying that the magnetic field causes deterrence to the cooling effect. The same conclusion may be reached from the concentration profiles of all three hnfs (see Figure 10).

The effect of suction/injection on AGE, CAE, and CGE hnfs is analyzed for suction parameters $S = -0.2, 0.0, 0.2$. For these parameters, the velocity, temperature, and concentration profiles are represented in Figures 11-13. For obvious reasons, the suction causes a decrease, and injection increases the velocity profile, irrespective of the type of hnf. Likewise, the temperature profile increases with suction and decreases with injection. When the wall suction ($S > 0$) is considered, the results imply a decrease in the boundary layer thickness and an increase in the fluid velocity. $S = 0$ represents a non-porous plate. For injection ($S < 0$), a contrary behavior is observed. However, the overall effect on these profiles of AGE, CAE, and CGE hybrid nanoparticles remains the same when compared to the effect of the Williamson parameter. The results indicate that the temperature decreases with increasing suction, which increases due to an increase in injection. Further, suction or injection effects are more or less similar in all three types of hnfs, *i.e.*, independent of the type of nanoparticles present in the fluid. We can see from Figure 13 that the concentration and its boundary layer thickness decrease with an increase in suction/injection parameter S. The tiny nature of different nanoparticles may receive a similar effect due to suction or injection. The decrease and increase in concentration profile with suction and injection, respectively, and in both cases, a decrease in concentration profile with the boundary layer thickness (Figure 1).

The influence of dimensional less parameter Q representing heat source ($Q > 0$)/sink ($Q < 0$) on the temperature and concentration profiles for AGE, CAE, and CGE hnfs are revealed in Figure 14 and Figure 15. These graphs indicate that the temperature is enhanced and the concentration profile is diminished with the increases in the values of Q. This is due to an increase in the thickness of the thermal boundary layer and a decrease in the heat transfer rate from the surface to the fluid. Mohamed R.Eid and Mohamed A. Nafe [38] observed similar results in MHD hnfs. Geethan Kumar *et al.* [42] have also observed an increase in the thickness of the thermal boundary layer of chemically reactive Williamson fluid.

It can be perceived from Figure 16 that the axial and transverse velocities of AGE, CAE, and CGE hnfs decrease as the porosity parameter K increases. The increase in porosity causes more permeability to the fluid along the z-direction, increasing the fluid velocity along the negative z-direction and causing the re-

duction of velocities. Contrarily, the porosity parameter manifests a rise in temperature and concentration profiles. **Figure 17** and **Figure 18** demonstrate that this effect is independent of the type of nanoparticles in the hnf mixture. As K increases, the net amount of decrease in velocity reduces, which will cause less growth in the temperature profile.

Figures 19-21 show the effect of volume fraction Φ_2 on axial and transverse velocities ($f'(\eta)$ and $g'(\eta)$), $\theta(\eta)$, and $\phi(\eta)$ profiles. As Φ_2 surges, the axial and transverse velocity profiles increase in the order of CGE, AGE, and CAE hnfs (**Figure 19**). Further, the increase of Φ_2 causes an increase in the resistance force within the fluids consisting of GaN nanoparticles in such a way that the temperature profiles exhibit the opposite trend (**Figure 20**), *i.e.*, in the order of AGE and CGE. The temperature profile of AGE remains below the temperature profile of CGE because the thermal conductivity boundary layer thickness of AGE decreases more than that of CGE. Also, the change in boundary layer thickness in CAE is not as much as AGE and CGE since it does not contain GaN nanoparticles. Lie group analysis of a Powell-Eyring nanofluids flow over a stretching surface by Hammed Abiodun Ogunseye *et al.* [52] has also given a similar conclusion on Al_2O_3-water nanofluids. **Figure 21** shows that the concentration profiles of CGE and AGE are more than that of CAE, and among the hnfs having GaN nanoparticles, CGE hnf has a higher concentration profile than that of AGE hnf. Kandasamy *et al.* [53] observed a similar result in Cu-water and SWCNT-water nanofluids. The decrease in concentration profile of SWCNT-water nanofluids is due to the higher diffusion boundary layer thickness possessed by SWCNT-water nanofluids when compared to Cu-water fluids since the CNTs have extraordinary [53]. Due to the nitride element present in GaN, CGE and AGE hnfs show higher concentration profiles than CAE hnf. Therefore, CGE and AGE are assigned lower diffusion boundary layer thicknesses than CAE hnf. Among CGE and AGE hnfs, the concentration profile of AGE hnf is less than CGE hnf, and AGE hnf may be assigned a higher diffusion boundary layer thickness than CGE. Further, CAE hnf is assigned with the highest diffusion boundary layer thickness than CGE and AGE as it shows the lower concentration profile among all the studied CGE, AGE, and CAE hnfs.

Figure 22 exhibits the effect of Prandtl number Pr on temperature profile $\theta(\eta)$ of CGE, AGE, and CAE hnfs. "Prandtl number Pr is defined as the ratio of momentum diffusivity to the thermal diffusivity." When the thermal diffusivity increases, Pr and temperature field depreciate [54]. This behavior is expected in most nanofluids and has also been observed by several researchers in nanofluids with different combinations of nanoparticles and base fluids [34] [55] [56]. Further, the graphical presentation given in **Figure 22** shows that the thermal diffusivities of CGE, AGE, and CAE hnfs, vary according to the relation CGE < CAE < AGE. The explanation for this relationship is that the sum of specific heat capacities and thermal conductivities of the nanoparticles mixed with the base fluid Ethylene glycol vary according to the descending order CGE > CAE > AGE.

Thermal radiation, the strength identified by a radiation parameter R, enhances the nanofluid temperature by thermal boundary layer thickness. Thermal radiation adds heat to the nanofluid, causing a rise in the fluid temperature. As a result of thermal radiation, the temperature field of a nanofluid improves with the increase in the parameter R. The change in temperature profile as a function of R for CGE, AGE, and CAE hnfs is presented in Figure 23. As expected, the variations in this figure showed improvement in the temperature profile with an increase in the thermal radiation parameter R. This means that all the hnfs absorb heat from the thermal radiation and increase the thermal boundary layer thicknesses and temperature. It is worth mentioning that heat energy absorption occurs among the fluid molecules by enhancing their vibrational energies proportional to the quantum of heat energy absorbed. With the increase in heat radiation, the content of heat absorbed by all CGE, AGE, and CAE hybrid nanofluids remains almost the same because the volume fraction of nanoparticles in each hnf is much less, and mostly the water molecules take part in the process of absorption.

Figure 24 depicts temperature profiles of CGE, AGE, and CAE hnfs, demonstrating the effect of Bi on heat dispersion. The temperature profile rises as the Biot number increases because the Biot number relates to internal conductive resistance, and the surface provides convective resistance. As the Biot number increases, so does the internal conductive resistance, increasing the cross-boundary layer thickness. And thus, the fluid temperature increases. Without abnormalities, the temperature profiles of the three hnfs increased with an increase in Biot number Bi. The variation of concentration field of CGE, AGE, and CAE with Schmidt number Sc is depicted the Figure 25. Schmidt number is "the ratio of momentum diffusivity to the Brownian diffusivity." The Brownian diffusivity parameter increases due to the random collision of molecules in nanofluid, which intern lowers the Sc. As a result, the concentration boundary layer thickness grows as Sc improves, decreasing the mass fraction field. From Figure 25, the nanoparticle concentration declines with the enhancement in Schmidt number in all the hnfs (CGE, CAE, AGE) because Sc is inverse proportion to the diffusion rate of mass [42]. Therefore, mass diffusion decreases as the Schmidt number increases in all the hybrid nanofluids under study.

"The stretching rate parameter a is the ratio of the transverse velocity to the axial velocity. In general, the porosity parameter reduces fluid velocity." It signifies the increase in the stretching parameter of the porous sheet, and the transverse velocity exceeds the axial velocity [42]. Henceforth, the rise in the value of a causes a rise in the transverse velocity and, simultaneously, a decrease in the axial velocity. This trend is shown graphically in Figure 26 for CGE, AGE, and CAE hybrid nanofluids. The stretching rate parameter a also causes a decrease in the temperature and concentration profiles (Figure 27 and Figure 28).

The influence of activation parameter E on the $\phi(\eta)$ of CGE, AGE, and CAE hybrid nanofluids is presented graphically in Figure 29. in fact, E is the energy that is sufficient to continue the chemical reaction and is known as "the

least amount of energy necessary to initiate and sustain a chemical reaction." In general, the rise in the activation energy causes an increase in the nanoparticle concentration. Aamir Hamid *et al.* [57] have studied the "Impacts of chemical reaction with activation energy on the unsteady flow of magneto-Williamson nanofluids and concluded that the increase in the destructive chemical reaction parameter $\sigma > 0$ tends to reduce the nanoparticle concentration profile" [57]. An increase in activation energy parameter E causes an impact on increasing the concentration profiles of all three hnfs.

According to Figure 30, the nanoparticle concentration in the hybrid nanofluid falls as the boundary layer thickness of the solute decreases due to an increase in the chemical reaction parameter σ. Diffusivity of the fluid varies due to changes in the intensity of chemical reaction, and thus the concentration declines. Kandasamy *et al.* [53] discovered that when the chemical reaction and buoyancy ratio increase, the concentration of water-based SWCNTs, Cu, and Al$_2$O$_3$ decreases, but the rate of mass transfer increases due to the combined impact of diffusion conductivity and kinematic viscosity of the nanoparticles. They also discovered that the diffusion boundary layer thickness of water-base Cu and SWCNTs increases faster than that of Al$_2$O$_3$-water as the chemical reaction progresses [53]. Figure 30 indicates that 1) the concentration profiles of CGE, AGE, and CAE hnfs decrease with the increase in the chemical reaction parameter σ and 2) the deviation in the profile geometry between two consecutive profiles decreases, gradually, as σ progresses. It could be due to a gradual decrease in the amount of fluid for the reaction or an increase in the chemical reaction boundary layer thickness.

6. Conclusions

A numerical analysis of a 3-D Williamson MHD fluid consisting of Ethylene glycol embedded with Cu-GaN, Al$_2$O$_3$-GaN, and Cu-GaN hybrid nanoparticles passed over a linearly stretching porous sheet with Suction/Injection, and Heat Source/Sink, Radiation, and Arrhenius activation energy addressed, and the results presented in the article. Various hydrodynamic profiles, numerical data of Skin friction coefficient, Nusselt number, and Sherwood numbers are estimated. The shooting technique algorithm based on the Runge-Kutta method was employed to secure the results. The results presented are:

- As the local Williamson parameter λ_1 increases, the axial and the transverse velocities decrease and increase, respectively, in the three CGE, AGE, and CAE hybrid nanofluids. The temperature profiles increase in the order of CGE, CAE, and AGE hybrid nanofluids indicating higher heat flow and a more significant concentration flow profile in CGE nanofluids than in the other two fluids.

- Axial and transverse velocities corresponding to AGE, CAE, and CGE hybrid nanofluids diminish with an increase in the magnetic field parameter. However, the changes observed in the variation of velocity profile with the Williamson parameter and magnetic field are the same and indicate that CGE

hybrid nanofluid is a better cooling agent among all three.

- The suction parameter ($S > 0$) causes a decrease in the boundary layer thickness and an increase in the fluid velocity. A contrary behavior occurs for injection ($S < 0$). The effect of suction/injection on AGE, CAE, and CGE is the same, *i.e.*, independent of the type of nanoparticles present in the fluid.

- As the parameter of heat source Q rises from the sink) to $+Q$ (source), the temperature profile is enhanced, and the concentration profile is diminished due to an increase in the thermal boundary layer thickness. A similar increase in temperature profile due to an increase in the thermal boundary layer thickness occurs in CGE, CAE, and AGE hybrid nanofluids with the increase in Radiation parameter.

- The x- and y-axis velocities and the related momentum boundary layer thickness in AGE, CAE, and CGE hybrid nanoparticles decrease as the porosity parameter K increases.

- Diffusion boundary layer thickness of CGE, CAE, and AGE hybrid nanofluids are in the order of CAE < CGE < AGE, implying that GaN nanoparticles enhance the diffusion boundary layer of a nanofluid.

- The increase in Prandtl number causes a decrease in the temperature profiles of CGE, CAE, and AGE hybrid nanofluids in the order CGE < CAE < AGE based on the order of thermal diffusivity variation CGE < CAE < AGE.

- The temperature profile of the three hybrid nanofluids increases with an increase in Biot number Bi, and mass diffusion decreases with an increased Schmidt number in all the hybrid nanofluids.

- The value of stretching rate parameter α causes a rise in the transverse velocity and lowers the axial velocity, the temperature, and concentration profiles of CGE, CAE, and AGE hnfs.

- An increase in activation energy parameter E shows an impact of increasing the concentration profiles of all the three hybrid nanoparticles

- As the "σ" progresses, 1) the concentration profiles of CGE, AGE, and CAE hybrid nanofluids decrease, and 2) the deviation in the profile geometry between two consecutive profiles decreases gradually, and it could be due to a gradual decrease in the amount of fluid available for reaction or an increase in the chemical reaction boundary layer thickness.

Acknowledgements

Authors' Information

M. Jyotshna is an Assistant Professor at the Department of Mathematics,

Maturi Venkata Subba Rao Engineering College (Affiliated to Osmania University) Nadergul, Hyderabad-501510, India. She is also a Researcher at the Department of Mathematics, University College of Science, Osmania University, Hyderabad-500007, India. Her research interests are Applied Mathematics and Nanofluids. **ORCID Number**: https://orcid.org/0000-0002-3657-6322.

V. Dhanalaxmi is a Professor of Mathematics at the University College of Technology, Osmania University. Hyderabad-500007, India. Her research interests are fluid mechanics and Applied Mathematics.

Conflicts of Interest

The authors declare no conflicts of interest.

References

[1] Sakiadis, B.C. (1961) Boundary-Layer Behavior on Continuous Solid Surfaces. II. Boundary-Layer Equations on a Continuous Flat Surface. *AIChE Journal*, **7**, 221-225. https://doi.org/10.1002/aic.690070211

[2] Crane, J. (1970) Flow past a Stretching Plate. *Kurze Mitteilungen-Brief Reports*, **21**, 645-647. https://doi.org/10.1007/BF01587695

[3] Masuda, H., Ebata, A., Teramae, K. and Hishinuma, N. (1993) Alteration of Thermal Conductivity and Viscosity of Liquid by Dispersing Ultra-Fine Particles. Dispersion of Al_2O_3, SiO_2 and TiO_2 Ultra-Fine Particles. *Netsu Bussei*, **7**, 227-233. https://doi.org/10.2963/jjtp.7.227

[4] Choi, S. (1998) Nanofluid Technology: Current Status and Future Research. Argonne National Lab, Argonne. http://www.ncbi.nlm.nih.gov/pubmed/11048%5Cnhttp://www.osti.gov/energycitations/product.biblio.jsp?osti_id=11048

[5] Hayat, T., Qayyum, S., Imtiaz, M. and Alsaedi, A. (2016) Comparative Study of Silver and Copper Water Nanofluids with Mixed Convection and Nonlinear Thermal Radiation. *International Journal of Heat and Mass Transfer*, **102**, 723-732. https://doi.org/10.1016/j.ijheatmasstransfer.2016.06.059

[6] Malik, M.Y., Bibi, M., Khan, F. and Salahuddin, T. (2016) Numerical Solution of Williamson Fluid Flow past a Stretching Cylinder and Heat Transfer with Variable Thermal Conductivity and Heat Generation/Absorption. *AIP Advances*, **6**, Article ID: 035101. https://doi.org/10.1063/1.4943398

[7] Kebede, T., Haile, E., Awgichew, G. and Walelign, T. (2020) Heat and Mass Transfer in Unsteady Boundary Layer Flow of Williamson Nanofluids. *Journal of Applied Mathematics*, **2020**, Article ID: 1890972. https://doi.org/10.1155/2020/1890972

[8] Sheikholeslami, M., Shehzad, S.A., Li, Z. and Shafee, A. (2018) Numerical Modeling for Alumina Nanofluid Magnetohydrodynamic Convective Heat Transfer in a Permeable Medium Using Darcy Law. *International Journal of Heat and Mass Transfer*, **127**, 614-622. https://doi.org/10.1016/j.ijheatmasstransfer.2018.07.013

[9] Eid, M.R. (2020) Effects of NP Shapes on Non-Newtonian Bio-Nanofluid Flow in Suction/Blowing Process with Convective Condition: Sisko Model. *Journal of Non-Equilibrium Thermodynamics*, **45**, 97-108. https://doi.org/10.1515/jnet-2019-0073

[10] Eid, M.R. and Al-Hossainy, A.F. (2020) Synthesis, DFT Calculations, and Heat Transfer Performance Large-Surface TiO_2: Ethylene Glycol Nanofluid and Coolant

Applications. *The European Physical Journal Plus*, **135**, 596.
https://doi.org/10.1140/epjp/s13360-020-00599-y

[11] Kotresh, M.J., Ramesh, G.K., Shashikala, V.K.R. and Prasannakumara, B.C. (2021) Assessment of Arrhenius Activation Energy in Stretched Flow of Nanofluid over a Rotating Disc. *Heat Transfer*, **50**, 2807-2828. https://doi.org/10.1002/htj.22006

[12] Ammani Kuttan, B., Manjunatha, S., Jayanthi, S. and Gireesha, B.J. (2020) Performance of Four Different Nanoparticles in Boundary Layer Flow over a Stretching Sheet in Porous Medium Driven by Buoyancy Force. *International Journal of Applied Mechanics and Engineering*, **25**, 1-10.
https://doi.org/10.2478/ijame-2020-0016

[13] Vinita, V. and Poply, V. (2019) Impact of Outer Velocity MHD Slip Flow and Heat Transfer of Nanofluid past a Stretching Cylinder. *Materials Today: Proceedings*, **26**, 3429-3435. https://doi.org/10.1016/j.matpr.2019.11.304

[14] Mondal, H., Das, S. and Kundu, P.K. (2020) Influence of an Inclined Stretching Cylinder over MHD Mixed Convective Nanofluid Flow Due to Chemical Reaction and Viscous Dissipation. *Heat Transfer*, **49**, 2183-2193.
https://doi.org/10.1002/htj.21714

[15] Mallikarjuna, H.B., Nirmala, T., Punith Gowda, R.J., Manghat, R. and Varun Kumar, R.S. (2021) Two-Dimensional Darcy-Forchheimer Flow of a Dusty Hybrid Nanofluid over a Stretching Sheet with Viscous Dissipation. *Heat Transfer*, **50**, 3934-3947.
https://doi.org/10.1002/htj.22058

[16] Khan, M.I. and Alzahrani, F. (2021) Free Convection and Radiation Effects in Nanofluid (Silicon Dioxide and Molybdenum Disulfide) with Second Order Velocity Slip, Entropy Generation, Darcy-Forchheimer Porous Medium. *International Journal of Hydrogen Energy*, **46**, 1362-1369. https://doi.org/10.1016/j.ijhydene.2020.09.240

[17] Al-Hossainy, A.F. and Eid, M.R. (2020) Structure, DFT Calculations and Heat Transfer Enhancement in [ZnO/PG+H$_2$O]C Hybrid Nanofluid Flow as a Potential Solar Cell Coolant Application in a Double-Tube. *Journal of Materials Science: Materials in Electronics*, **31**, 15243-15257.
https://doi.org/10.1007/s10854-020-04089-w

[18] Ramzan, M., Gul, H. and Zahri, M. (2020) Darcy-Forchheimer 3D Williamson Nanofluid Flow with Generalized Fourier and Fick's Laws in a Stratified Medium. *Bulletin of the Polish Academy of Sciences: Technical Sciences*, **68**, 327-335.

[19] Sriharan, G., Harikrishnan, S. and Ali, H.M. (2021) Experimental Investigation on the Effectiveness of MHTHS Using Different Metal Oxide-Based Nanofluids. *Journal of Thermal Analysis and Calorimetry*, **143**, 1251-1260.
https://doi.org/10.1007/s10973-020-09779-5

[20] Rashid, U. and Ibrahim, A. (2020) Impacts of Nanoparticle Shape on Al-Water Nanofluid Flow and Heat Transfer over a Non-Linear Radically Stretching Sheet. *Advances in Nanoparticles*, **9**, 23-39. https://doi.org/10.4236/anp.2020.91002

[21] Gupta, S., Kumar, D. and Singh, J. (2019) Magnetohydrodynamic Three-Dimensional Boundary Layer Flow and Heat Transfer of Water-Driven Copper and Alumina Nanoparticles Induced by Convective Conditions. *International Journal of Modern Physics B*, **33**, Article ID: 1950307. https://doi.org/10.1142/S0217979219503077

[22] Eastman, J.A., Choi, S.U.S., Li, S., Yu, W. and Thompson, L.J. (2001) Anomalously Increased Effective Thermal Conductivities of Ethylene Glycol-Based Nanofluids Containing Copper Nanoparticles. *Applied Physics Letters*, **78**, 718-720.
https://doi.org/10.1063/1.1341218

[23] Nogueira, É. (2020) Efficiency and Effectiveness Concepts Applied in Shell and

Tube Heat Exchanger Using Ethylene Glycol-Water Based Fluid in the Shell with Nanoparticles of Copper Oxide (CuO). *Journal of Materials Science and Chemical Engineering*, **8**, 1-12. https://doi.org/10.4236/msce.2020.88001

[24] Ohno, Y. and Kuzuhara, M. (2001) Application of GaN-Based Heterojunction FETs for Advanced Wireless Communication. *IEEE Transactions on Electron Devices*, **48**, 517-523. https://doi.org/10.1109/16.906445

[25] Zhao, Z., *et al*. (2004) Grain-Size Effects on the Ferroelectric Behavior of Dense Nanocrystalline $BaTiO_3$ Ceramics. *Physical Review B: Condensed Matter and Materials Physics*, **70**, Article ID: 024107. https://doi.org/10.1103/PhysRevB.70.024107

[26] Hreniak, D., *et al*. (2004) The Size-Effect on Luminescence Properties of $BaTiO_3:Eu^{3+}$ Nanocrystallites Prepared by the Sol-Gel Method. *Journal of Alloys and Compounds*, **380**, 348-351. https://doi.org/10.1016/j.jallcom.2004.03.012

[27] Hreniak, D. and Stręk, W. (2002) Synthesis and Optical Properties of Nd^{3+}-Doped Y $3Al_5O_{12}$ Nanoceramics. *Journal of Alloys and Compounds*, **341**, 183-186. https://doi.org/10.1016/S0925-8388(02)00067-1

[28] Kameswaran, P.K., Sibanda, P. and Murti, A.S.N. (2013) Nanofluid Flow over a Permeable Surface with Convective Boundary Conditions and Radiative Heat Transfer. *Mathematical Problems in Engineering*, **2013**, Article ID: 201219. https://doi.org/10.1155/2013/201219

[29] Bachok, N., Ishak, A. and Pop, I. (2012) Boundary Layer Stagnation-Point Flow and Heat Transfer over an Exponentially Stretching/Shrinking Sheet in a Nanofluid. *International Journal of Heat and Mass Transfer*, **55**, 8122-8128. https://doi.org/10.1016/j.ijheatmasstransfer.2012.08.051

[30] Mandal, G. (2016) Convective-Radiative Heat Transfer of Micropolar Nanofluid over a Vertical Non-Linear Stretching Sheet. *Journal of Nanofluids*, **5**, 852-860. https://doi.org/10.1166/jon.2016.1265

[31] Mandal, S. and Shit, G.C. (2022) Entropy Analysis of Unsteady MHD Three-Dimensional Flow of Williamson Nanofluid over a Convectively Heated Stretching Sheet. *Heat Transfer*, **51**, 2034-2062. https://doi.org/10.1002/htj.22387

[32] Swain, K. and Mahanthesh, B. (2021) Thermal Enhancement of Radiating Magneto-Nanoliquid with Nanoparticles Aggregation and Joule Heating: A Three-Dimensional Flow. *Arabian Journal for Science and Engineering*, **46**, 5865-5873. https://doi.org/10.1007/s13369-020-04979-5

[33] Siddiqui, A.A. and Sheikholeslami, M. (2018) TiO_2-Water Nanofluid in a Porous Channel under the Effects of an Inclined Magnetic Field and Variable Thermal Conductivity. *Applied Mathematics and Mechanics* (*English Ed.*), **39**, 1201-1216. https://doi.org/10.1007/s10483-018-2359-6

[34] Nayak, M.K., Prakash, J., Tripathi, D. and Pandey, V.S. (2019) 3D Radiative Convective Flow of ZnO-SAE50 Nano-Lubricant in Presence of Varying Magnetic Field and Heterogeneous Reactions. *Propulsion and Power Research*, **8**, 339-350. https://doi.org/10.1016/j.jppr.2019.10.002

[35] Yacob, N.A., Dasman, A. and Ahmad, S. (2018) Regional Conference on Science, Technology and Social Sciences (RCSTSS 2016). Springer, Berlin. https://doi.org/10.1007/978-981-13-0074-5

[36] Ahmad, S.N., *et al*. (2021) Fractional Model for MHD Flow of Casson Fluid with Cadmium Telluride Nanoparticles Using the Generalized Fourier's Law. *Scientific Reports*, **11**, Article No. 16117. https://doi.org/10.1038/s41598-021-95528-z

[37] Sreedevi, P. and Sudarsana Reddy, P. (2022) Effect of Magnetic Field and Thermal Radiation on Natural Convection in a Square Cavity Filled with TiO_2 Nanoparticles

Using Tiwari-Das Nanofluid Model. *Alexandria Engineering Journal*, **61**, 1529-1541. https://doi.org/10.1016/j.aej.2021.06.055

[38] Eid, M.R. and Nafe, M.A. (2022) Thermal Conductivity Variation and Heat Generation Effects on Magneto-Hybrid Nanofluid Flow in a Porous Medium with Slip Condition. *Waves in Random and Complex Media*, **32**, 1103-1127. https://doi.org/10.1080/17455030.2020.1810365

[39] Jyotshna, M. and Dhanalaxmi, V. (2022) Impact of Activation Energy and Heat Source/Sink on 3D Flow of Williamson Nanofluid with GaN Nanoparticles over a Stretching Sheet. *European Journal of Mathematics and Statistics*, **3**, 16-29. https://doi.org/10.24018/ejmath.2022.3.5.133

[40] Nadeem, S., Hussain, S.T. and Lee, C. (2013) Flow of a Williamson Fluid over a Stretching Sheet. *Brazilian Journal of Chemical Engineering*, **30**, 619-625. https://doi.org/10.1590/S0104-66322013000300019

[41] Shawky, H.M., Eldabe, N.T.M., Kamel, K.A. and Abd-Aziz, E.A. (2019) MHD Flow with Heat and Mass Transfer of Williamson Nanofluid over Stretching Sheet through Porous Medium. *Microsystem Technologies*, **25**, 1155-1169. https://doi.org/10.1007/s00542-018-4081-1

[42] Geethan, K.S., Varma, S.V.K., Kiran Kumar, R.V.M.S.S., Raju, C.S.K., Shehzad, S.A. and Bashir, M.N. (2019) Three-Dimensional Hydromagnetic Convective Flow of Chemically Reactive Williamson Fluid with Non-Uniform Heat Absorption and Generation. *International Journal of Chemical Reactor Engineering*, **17**, 1-17. https://doi.org/10.1515/ijcre-2018-0118

[43] Bilal, S., Khalil-ur-Rehman, Malik, M.Y., Hussain, A. and Khan, M. (2017) Effects of Temperature Dependent Conductivity and Absorptive/Generative Heat Transfer on MHD Three Dimensional Flow of Williamson Fluid Due to Bidirectional Non-Linear Stretching Surface. *Results in Physics*, **7**, 204-212. https://doi.org/10.1016/j.rinp.2016.11.063

[44] Sultan, F., Khan, W.A., Ali, M., Shahzad, M., Irfan, M. and Khan, M. (2019) Theoretical Aspects of Thermophoresis and Brownian Motion for Three-Dimensional Flow of the Cross Fluid with Activation Energy. *Pramana—Journal of Physics*, **92**, Article No. 21. https://doi.org/10.1007/s12043-018-1676-0

[45] Khashi'ie, N.S., Arifin, N.M., Pop, I., Nazar, R., Hafidzuddin, E.H. and Wahi, N. (2020) Three-Dimensional Hybrid Nanofluid Flow and Heat Transfer past a Permeable Stretching/Shrinking Sheet with Velocity Slip and Convective Condition. *Chinese Journal of Physics*, **66**, 157-171. https://doi.org/10.1016/j.cjph.2020.03.032

[46] Alaidrous, A.A. and Eid, M.R. (2020) 3-D Electromagnetic Radiative Non-Newtonian Nanofluid Flow with Joule Heating and Higher-Order Reactions in Porous Materials. *Scientific Reports*, **10**, Article No. 14513. https://doi.org/10.1038/s41598-020-71543-4

[47] Nandi, S. and Kumbhakar, B. (2021) Viscous Dissipation and Chemical Reaction Effects on Tangent Hyperbolic Nanofluid Flow past a Stretching Wedge with Convective Heating and Navier's Slip Conditions. *Iranian Journal of Science and Technology, Transaction of Mechanical Engineering*, **46**, 379-397. https://doi.org/10.1007/s40997-021-00437-1

[48] Laxmi, T.V. and Shankar, B. (2016) Effect of Nonlinear Thermal Radiation on Boundary Layer Flow of Viscous Fluid over Nonlinear Stretching Sheet with Injection/Suction. *Journal of Applied Mathematics and Physics*, **4**, 307-319. https://doi.org/10.4236/jamp.2016.42038

[49] Srinivasulu, T. and Goud, B.S. (2021) Effect of Inclined Magnetic Field on Flow,

Heat and Mass Transfer of Williamson Nanofluid over a Stretching Sheet. *Case Studies in Thermal Engineering*, **23**, Article ID: 100819.
https://doi.org/10.1016/j.csite.2020.100819

[50] Rushi, B., Sivaraj, K.R. and Prakash, J. (2018) Lecture Notes in Mechanical Engineering Advances in Fluid Dynamics. Springer, Berlin.
http://www.springer.com/series/11693

[51] Oyelakin, I.S., Lalramneihmawii, P., Mondal, S., Nandy, S.K. and Sibanda, P. (2020) Thermophysical Analysis of Three-Dimensional Magnetohydrodynamic Flow of a Tangent Hyperbolic Nanofluid. *Engineering Reports*, **2**, e12144.
https://doi.org/10.1002/eng2.12144

[52] Ogunseye, H.A., Mondal, H., Sibanda, P. and Mambili-Mamboundou, H. (2020) Lie Group Analysis of a Powell-Eyring Nanofluid Flow over a Stretching Surface with Variable Properties. *SN Applied Sciences*, **2**, Article No. 115.
https://doi.org/10.1007/s42452-019-1852-y

[53] Kandasamy, R., Mohamad, R. and Ismoen, M. (2016) Impact of Chemical Reaction on Cu, Al_2O_3 and SWCNTs-Nanofluid Flow under Slip Conditions. *Engineering Science and Technology, an International Journal*, **19**, 700-709.
https://doi.org/10.1016/j.jestch.2015.11.011

[54] Sajid, T., Tanveer, S., Sabir, Z. and Guirao, J.L.G. (2020) Impact of Activation Energy and Temperature-Dependent Heat Source/Sink on Maxwell-Sutterby Fluid. *Mathematical Problems in Engineering*, **2020**, Article ID: 5251804.
https://doi.org/10.1155/2020/5251804

[55] Hayat, T., Shah, F., Khan, M.I., Khan, M.I. and Alsaedi, A. (2018) Entropy Analysis for Comparative Study of Effective Prandtl Number and without Effective Prandtl Number via γAl_2O_3-H_2O and γAl_2O_3-$C_2H_6O_2$ Nanoparticles. *Journal of Molecular Liquids*, **266**, 814-823. https://doi.org/10.1016/j.molliq.2018.06.029

[56] Hussain, S.T., Nadeem, S. and Ul Haq, R. (2014) Model-Based Analysis of Micropolar Nanofluid Flow over a Stretching Surface. *The European Physical Journal Plus*, **129**, Article No. 161. https://doi.org/10.1140/epjp/i2014-14161-8

[57] Hamid, A., Hashim and Khan, M. (2018) Impacts of Binary Chemical Reaction with Activation Energy on Unsteady Flow of Magneto-Williamson Nanofluid. *Journal of Molecular Liquids*, **262**, 435-442. https://doi.org/10.1016/j.molliq.2018.04.095

Nomenclature

E_a Activation energy parameter

S_c Schmidt number

A_1 First Rivlin-Erickson tensor

B_o Magnetic field strength

c_p Specific heat at constant Pressure

σ^* Stefan Boltzmann constant

D_B Diffusion coefficient

k^* Mean absorption coefficient

K_o Chemical reaction constant

K_p Permeability of the porous medium

P_r Prandtl number

Q_o Heat source/sink

α_{nf} Thermal diffusivity

α_{nf} Thermal diffusivity

λ_1 & λ_2 Williamson parameters

μ_0 Limiting viscosity at zero shear rate

μ_∞ Limiting viscosity at infinity shear rate

μ_{nf} Dynamic viscosity of the nanofluid

ρ_{nf} Nanofluid density

a Stretching ratio parameter

C Concentration of the fluid

E Activation energy parameter

I Identity vector

k Boltzmann constant

m Fitted rate constant

M Magnetic parameter

$\dot{p}$ Pressure

Q Heat source/sink parameter

R Radiation parameter

S Suction/injection

$\dot{S}$ Cauchy stress tensor

T Temperature of the fluid

Γ Time constant

δ Temperature difference parameter

ρ Density

σ Chemical reaction parameter

σ Electric conductivity

τ Extra stress tensor

Γ Williamson fluid parameter